




















SUPER

V. ALMA continuum observations of $z \sim 2$ AGN and the elusive evidence of outflows influencing star formation

I. Lamperti^{1,2,3} , C. M. Harrison⁴ , V. Mainieri¹ , D. Kakkad^{5,6} , M. Perna^{3,7} , C. Circosta², J. Scholtz⁸ , S. Carniani⁹, C. Cicone¹⁰ , D. M. Alexander¹¹, M. Bischetti¹² , G. Calistro Rivera¹, C.-C. Chen¹³ , G. Cresci⁷ , C. Feruglio¹², F. Fiore¹², F. Mannucci⁷ , A. Marconi^{14,7} , L. N. Martínez-Ramírez^{1,15}, H. Netzer¹⁶ , E. Piconcelli¹⁷ , A. Puglisi¹¹ , D. J. Rosario¹¹ , M. Schramm¹⁸ , G. Vietri¹⁹ , C. Vignali^{20,21}, and L. Zappacosta¹⁷ 

¹ European Southern Observatory, Karl-Schwarzschild-Str. 2, 85748 Garching bei München, Germany
e-mail: isabellalamperti@gmail.com

² Department of Physics and Astronomy, University College London, Gower Street, London WC1E 6BT, UK

³ Centro de Astrobiología (CAB, CSIC-INTA), Departamento de Astrofísica, Ctra. de Ajalvir Km. 4, 28850 Torrejón de Ardoz, Madrid, Spain

⁴ School of Mathematics, Statistics and Physics, Herschel Building, Newcastle University, Newcastle upon Tyne NE1 7RU, UK
e-mail: christopher.harrison@newcastle.ac.uk

⁵ European Southern Observatory, Alonso de Cordova 3107, Casilla 19, Santiago 19001, Chile

⁶ Department of Physics, University of Oxford, Denys Wilkinson Building, Keble Road, Oxford OX1 3RH, UK

⁷ INAF – Osservatorio Astrofisico di Arcetri, Largo E. Fermi 5, 50125 Firenze, Italy

⁸ Chalmers University of Technology, Department of Earth and Space Sciences, Onsala Space Observatory, 43992 Onsala, Sweden

⁹ Scuola Normale Superiore, Piazza dei Cavalieri 7, 56126 Pisa, Italy

¹⁰ Institute of Theoretical Astrophysics, University of Oslo, PO Box 1029, Blindern 0315, Oslo, Norway

¹¹ Centre for Extragalactic Astronomy, Department of Physics, Durham University, South Road, Durham DH1 3LE, UK

¹² INAF – Osservatorio Astronomico di Trieste, Via G. B. Tiepolo 11, 34143 Trieste, Italy

¹³ Academia Sinica Institute of Astronomy and Astrophysics (ASIAA), No. 1, Sec. 4, Roosevelt Rd., Taipei 10617, Taiwan

¹⁴ Dipartimento di Fisica e Astronomia, Università di Firenze, Via G. Sansone 1, 50019 Sesto Fiorentino, Firenze, Italy

¹⁵ Escuela de Física – Universidad Industrial de Santander, 680002 Bucaramanga, Colombia

¹⁶ School of Physics and Astronomy, Tel-Aviv University, Tel-Aviv 69978, Israel

¹⁷ INAF – Osservatorio Astronomico di Roma, Via di Frascati 33, 00078 Monte Porzio Catone, Italy

¹⁸ Graduate School of Science and Engineering, Saitama Univ. 255 Shimo-Okubo, Sakura-ku, Saitama City, Saitama 338-8570, Japan

¹⁹ INAF IASF-Milano, Via Alfonso Corti 12, 20133 Milano, Italy

²⁰ Dipartimento di Fisica e Astronomia, Alma Mater Studiorum, Università degli Studi di Bologna, Via Gobetti 93/2, 40129 Bologna, Italy

²¹ INAF – Osservatorio di Astrofisica e Scienza dello Spazio di Bologna, Via Gobetti 93/3, 40129 Bologna, Italy

Received 21 May 2021 / Accepted 30 August 2021

ABSTRACT

We study the impact of active galactic nuclei (AGN) ionised outflows on star formation in high-redshift AGN host galaxies, by combining near-infrared integral field spectroscopic (IFS) observations, mapping the $H\alpha$ emission and $[\text{O III}]\lambda 5007$ outflows, with matched-resolution observations of the rest-frame far-infrared (FIR) emission. We present high-resolution ALMA Band 7 observations of eight X-ray selected AGN ($L_{2-10\text{keV}} = 10^{43.8} - 10^{45.2} \text{ erg s}^{-1}$) at $z \sim 2$ from the SUPER (SINFONI Survey for Unveiling the Physics and Effect of Radiative feedback) sample, targeting the observed-frame $870 \mu\text{m}$ (rest-frame $\sim 260 \mu\text{m}$) continuum at $\sim 2 \text{ kpc}$ ($0.2''$) spatial resolution. The targets were selected among the SUPER AGN with an $[\text{O III}]$ detection in the IFS maps and with a detection in the FIR photometry. We detected six out of eight targets with signal-to-noise ratio $S/N \geq 10$ in the ALMA maps, from which we measured continuum flux densities in the range $0.27 - 2.58 \text{ mJy}$ and FIR half-light radii (R_e) in the range $0.8 - 2.1 \text{ kpc}$. The other two targets were detected with S/N of 3.6 and 5.9, which are insufficient for spatially resolved analysis. The FIR R_e of our sample are comparable to other AGN and star-forming galaxies at a similar redshift from the literature. However, combining our sample with the literature samples, we find that the mean FIR size in X-ray AGN ($R_e = 1.16 \pm 0.11 \text{ kpc}$) is slightly smaller than in non-AGN ($R_e = 1.69 \pm 0.13 \text{ kpc}$). From spectral energy distribution fitting, we find that the main contribution to the $260 \mu\text{m}$ flux density is dust heated by star formation, with $\leq 4\%$ contribution from AGN-heated dust and $\leq 1\%$ from synchrotron emission. The majority of our sample show different morphologies for the FIR (mostly due to reprocessed stellar emission) and the ionised gas emission ($H\alpha$ and $[\text{O III}]$, mostly due to AGN emission). This could be due to the different locations of dust and ionised gas, the different sources of the emission (stars and AGN), or the effect of dust obscuration. We are unable to identify any residual $H\alpha$ emission, above that dominated by AGN, that could be attributed to star formation. Under the assumption that the FIR emission is a reliable tracer of obscured star formation, we find that the obscured star formation activity in these AGN host galaxies is not clearly affected by the ionised outflows. However, we cannot rule out that star formation suppression is happening on smaller spatial scales than the ones we probe with our observations ($< 2 \text{ kpc}$) or on different timescales.

Key words. galaxies: star formation – galaxies: Seyfert – galaxies: active – galaxies: ISM

1. Introduction

Super-massive black holes (SMBHs) in the centre of galaxies have phases of intense accretion of material, during which they become very luminous and are identified as active galactic nuclei (AGN). AGN release large amounts of energy into the host galaxies ($\sim 10\%$ of the rest-mass energy of the accreted material, Shapiro et al. 1983; Marconi et al. 2004) and therefore have the potential to influence the properties of the interstellar medium (ISM) and ultimately its star formation rate (SFR). This phenomenon is called AGN feedback (e.g. Fabian 2012; King & Pounds 2015; Harrison 2017). Simulations of galaxy formation require AGN feedback in massive galaxies (stellar masses $> 10^{10} M_{\odot}$) in order to match many observables, such as the evolution of galaxy sizes (e.g. Choi et al. 2018), the galaxy colour bi-modality (Trayford et al. 2016), and the lack of very massive galaxies in the most massive galaxy haloes (Somerville et al. 2008; Behroozi et al. 2013).

A viable AGN feedback mechanism is represented by fast winds ($> 1000 \text{ km s}^{-1}$) originating from the AGN accretion disk, or by collimated radio jets, both of which can impact the surrounding gas, generating outflows which propagate to large distances into the host galaxy (e.g. King 2003; Mukherjee et al. 2018; Costa et al. 2020). These outflows can potentially heat the ISM and also expel gas from the host galaxy (Ishibashi & Fabian 2016; Zubovas 2018).

AGN outflows have been detected at different scales, extending from a few parsecs to kiloparsecs (e.g. Storchi-Bergmann et al. 2010; Veilleux et al. 2013; Cresci et al. 2015a; Feruglio et al. 2015; Kakkad et al. 2016, 2020; McElroy et al. 2016; Rupke et al. 2017; Jarvis et al. 2019; Marasco et al. 2020; Vietri et al. 2018, 2020). In addition, outflows have been observed in multiple gas phases: neutral and ionised as well as atomic and molecular (Cicone et al. 2018).

Understanding whether these outflows are able to have an impact on star formation is crucial for testing and refining the aforementioned simulations, which include a variety of different models of ‘AGN feedback’. This impact can be particularly important for galaxies at redshift $z \sim 2$, which corresponds to the peak of star formation and AGN activity in the Universe (e.g. Shankar et al. 2009; Madau & Dickinson 2014; Tacconi et al. 2020).

To study the impact of AGN outflows on star formation, one possibility is to use spatially resolved observations to map the distribution of both the outflows and the star-forming regions and look for spatial correlations or anti-correlations, which can indicate signatures of star formation enhancement (‘positive feedback’) or suppression (‘negative feedback’) (Cresci & Maiolino 2018, and references therein). Using integral field spectroscopy (IFS) at rest-frame optical wavelengths, several studies investigate the impact of ionised outflows, traced by $[\text{O III}]\lambda 5007$ ($[\text{O III}]$ hereafter), on star formation in AGN host galaxies and found evidence of both positive and negative feedback (e.g. Cano-Díaz et al. 2012; Cresci et al. 2015a; Carniani et al. 2016; Maiolino et al. 2017; Gallagher et al. 2019; Perna et al. 2020). However, the interpretation of some of these observations may not be trivial (see Scholtz et al. 2020, 2021). For example, assessing the impact of outflows on star formation can be complicated by the fact that common SFR tracers (e.g. the $\text{H}\alpha$ emission line) are affected by dust extinction (Madau et al. 1996; Casey et al. 2014; Whitaker et al. 2014). In some objects, the UV and $\text{H}\alpha$ emission could be completely hidden by the dust (e.g. Hodge et al. 2016; Chen et al. 2017; Puglisi et al. 2017). Thus, to have a complete view of the star formation in the host

galaxy, it is crucial to also have information about the dust-obscured star formation traced by the far-infrared (FIR) emission (e.g. Whitaker et al. 2014; Brusa et al. 2018; Scholtz et al. 2020; Bouwens et al. 2020).

High-resolution observations from the Atacama Large Millimeter/submillimeter Array (ALMA) have been used to measure the FIR sizes of high-redshift star-forming galaxies (e.g. Ikarashi et al. 2015; Simpson et al. 2015; Hodge et al. 2016; Gullberg et al. 2019; Puglisi et al. 2019; Cheng et al. 2020). Several studies found the rest-frame FIR sizes of star-forming galaxies at $z > 1$ to be smaller than the rest-frame optical sizes (e.g. Chen et al. 2015; Barro et al. 2016; Tadaki et al. 2017; Fujimoto et al. 2017, 2018; Elbaz et al. 2018; Calistro Rivera et al. 2018; Lang et al. 2019). A possible interpretation is that the central compact dusty star-forming component is related to the formation of the bulge (Fujimoto et al. 2017). Alternatively, Popping et al. (2021) suggested, based on simulations, that the larger rest-frame optical sizes could be due to higher dust-obscuration in the central region of galaxies, which artificially increases the ratio between the derived optical and FIR sizes. It is still unclear whether the presence of an AGN can affect (or is related to) the FIR size of the host galaxy. For example, Chang et al. (2020) studied a sample of seven AGN and 20 non-AGN at $z \sim 1$ and found that obscured IR-selected AGN have smaller FIR sizes (median size $R_e = 0.76 \pm 0.48 \text{ kpc}$) than non-AGN (median size $R_e = 1.62 \pm 0.50 \text{ kpc}$) at the same redshift and stellar mass. On the other hand, Harrison et al. (2016a) measured the FIR sizes of a sample of five X-ray selected AGN at $z \sim 1.5\text{--}4.5$ and found that their FIR sizes (FWHM size 1–3 kpc, median 1.8 kpc) are comparable to the sizes of sub-millimetre galaxies (SMGs) at the same redshift (median FWHM size $2.4 \pm 0.2 \text{ kpc}$).

This paper is part of a series of papers from SUPER¹ (SINFONI Survey for Unveiling the Physics and Effects of Radiative feedback, Circosta et al. 2018), an ESO large programme which aims to investigate the outflows properties of $z \sim 2$ X-ray AGN. The high resolution ($\sim 0.2\text{--}0.3''$, corresponding to $\sim 2 \text{ kpc}$) of the IFS SINFONI observations is critical to resolve the morphology of the ionised outflow (Kakkad et al. 2020) and connect it with the star formation properties of the host galaxy. In this work, we study the impact of AGN ionised outflows on both obscured and unobscured star formation in a sub-sample of eight SUPER AGN. We combine SINFONI IFS observations, to map the $\text{H}\alpha$ emission and $[\text{O III}]$ outflows, with matched-resolution ALMA observations of the continuum FIR emission at $\lambda_{\text{obs}} \sim 870 \mu\text{m}$ ($\lambda_{\text{rest}} \sim 260 \mu\text{m}$).

The paper is organised as follows. In Sect. 2, we describe the selection criteria and the general properties of the sample. In Sect. 3, we present the ALMA data and the analysis to extract the information about the FIR sizes and flux densities. Section 4 describes the SINFONI $\text{H}\alpha$ and $[\text{O III}]$ data. In Sect. 5 we present our results. First, we investigate the origin of the FIR emission in our targets (Sect. 5.1). Then, we compare the FIR sizes with other samples from the literature (Sect. 5.2). Finally, we compare the spatial distribution of the FIR continuum with the $\text{H}\alpha$ and $[\text{O III}]$ emission, as well as with the ionised outflows (Sects. 5.3 and 5.4). In Sect. 6, we summarise the main results and our conclusions.

Throughout this work, we assume wavelength in vacuum and a cosmological model with $\Omega_{\Lambda} = 0.7$, $\Omega_{\text{M}} = 0.3$, and $H_0 = 70 \text{ km s}^{-1} \text{ Mpc}^{-1}$.

¹ <http://www.super-survey.org>

Table 1. Properties of the sample.

Field	ID	RA	Dec	z	AGN	$\log M_*$	SFR	$\log L_{\text{bol}}$	$\log L_{2-10\text{keV}}$	$\log N_{\text{H}}$
(1)	(2)	[deg]	[deg]	(5)	type	[$\log M_{\odot}$]	[$M_{\odot}\text{yr}^{-1}$]	[erg s^{-1}]	[erg s^{-1}]	[cm^{-2}]
XMM-XXL	X_N_81_44	34.378942	-4.306572	2.311	BL	10.89 ± 0.25	173 ± 92	46.80 ± 0.03	$44.77^{+0.07}_{-0.09}$	<21.86
CDF-S	XID36	52.961556	-27.784281	2.259	NL	10.72 ± 0.08	186 ± 9	45.70 ± 0.06	$43.84^{+0.31}_{-0.63}$	>24.10
CDF-S	XID419	53.097649	-27.715270	2.145	NL	10.89 ± 0.02	44 ± 2	45.54 ± 0.05	$43.84^{+0.29}_{-0.44}$	$24.28^{+0.19}_{-0.31}$
COSMOS	cid_1057	149.812485	2.111014	2.214	NL	10.99 ± 0.08	64 ± 7	45.91 ± 0.06	$44.53^{+0.26}_{-0.30}$	$23.98^{+0.24}_{-0.28}$
COSMOS	cid_346	149.930878	2.118734	2.219	BL	10.67 ± 0.37	380 ± 29	46.66 ± 0.02	$44.47^{+0.08}_{-0.09}$	$23.05^{+0.17}_{-0.19}$
COSMOS	cid_451	150.002533	2.258629	2.450	NL	11.21 ± 0.05	48 ± 19	46.44 ± 0.07	$45.18^{+0.23}_{-0.19}$	$23.87^{+0.19}_{-0.15}$
COSMOS	cid_1205	150.010696	2.332968	2.255	BL ^(a)	11.16 ± 0.22	88 ± 16	45.75 ± 0.17	$44.25^{+0.21}_{-0.23}$	$23.50^{+0.27}_{-0.27}$
COSMOS	cid_1143	150.036819	2.257776	2.492	NL	10.82 ± 0.04	8 ± 2	44.85 ± 0.12	$44.83^{+0.43}_{-0.36}$	$24.01^{+0.77}_{-0.29}$

Notes. All quantities are taken from [Circosta et al. \(2018\)](#), except for the SFRs and stellar masses which have been derived from the SED fitting including the Band 7 fluxes presented in this paper (see Sect. 3.4). (1) Field where the targets are located. (2) Source identification number from the catalogues corresponding to each field. (3) RA and (4) Dec of the optical counterpart. (5) Spectroscopic redshift. (6) AGN classification as broad line (BL) or narrow line (NL) objects according to the optical spectra. (7) Host galaxy stellar mass and 1σ error. (8) SFR from the 8–1000 μm FIR luminosity and 1σ error. (9) AGN bolometric luminosity and 1σ error, derived from SED fitting. (10) Absorption-corrected X-ray luminosity in the hard band (2–10 keV) and 90% confidence level error. (11) Absorbing hydrogen column density and 90% confidence level error, derived from either X-ray spectral fitting or hardness-ratio (see [Circosta et al. 2018](#)). ^(a)cid_1205 was previously reported as a NL target in [Circosta et al. \(2018\)](#), but it is now classified as a BL target based on the presence of BLR emission in the $\text{H}\alpha$ line in the K -band SINFONI spectrum ([Kakkad et al. 2020](#)).

2. Sample

The sample studied in this paper consists of eight AGN with ALMA Band 7 continuum observations, which have been selected from the SUPER parent sample. The sample selection of SUPER is described in detail in [Circosta et al. \(2018\)](#). In brief, the 39 SUPER AGN were selected in the X-rays from various surveys, by adopting as a threshold an absorption-corrected X-ray luminosity of $L_{\text{X}} \geq 10^{42} \text{ erg s}^{-1}$, to exclude sources where the X-ray emission may come from star formation ([Aird et al. 2017](#)). The SUPER sample covers the redshift range $z = 2-2.5$ and spans a wide range of AGN bolometric luminosities² ($\sim 10^{44}-10^{48} \text{ erg s}^{-1}$) and X-ray luminosities ($L_{2-10\text{keV}} \sim 10^{43}-10^{46} \text{ erg s}^{-1}$). To select the sub-sample to be observed with ALMA, we considered all the SUPER objects with at least one photometric detection, based on the photometry we had in hand (i.e. a signal-to-noise $S/N > 3$ in the catalogue from [Circosta et al. 2018](#)) in the FIR (i.e. observed wavelength in the range 70–870 μm), to be able to properly assess the emission process at 870 μm (observed wavelength), and with [O III] detections in the completed IFS data at the time of the proposal (April 2018), to be able to investigate the impact of [O III] outflows on the dust-obscured star formation. The eight SUPER targets that satisfied these criteria were selected for the ALMA observations.

Our sample includes five AGN from the COSMOS-Legacy survey ([Civano et al. 2016](#); [Marchesi et al. 2016](#)), two from the *Chandra* Deep Field South (CDF-S, [Luo et al. 2017](#)), and one from the wide-area *XMM-Newton* XXL survey ([Pierre et al. 2016](#)). A summary of the sample characteristics is provided in Table 1.

Given the selection criteria based on the FIR and [O III] properties described above, it is important to consider how this sub-sample is representative of the parent population of the SUPER survey. Figure 1 shows the AGN bolometric luminosities (L_{bol}) and hydrogen column densities (N_{H}) for the total SUPER sample, with the ALMA targets highlighted in orange. Bolometric luminosities are derived from spectral energy distribution (SED)

fitting and N_{H} from the analysis of the X-ray spectra (for more details see [Circosta et al. 2018](#)). The ALMA targets have bolometric luminosities in the range $\log(L_{\text{bol}}/[\text{erg s}^{-1}]) = 44.9-46.8$, with median $\log(L_{\text{bol}}/[\text{erg s}^{-1}]) = 45.8$. They are therefore representative in terms of bolometric luminosities of the parent SUPER sample (median $\log L_{\text{bol}}/[\text{erg s}^{-1}] = 46.0$ and interquartile range $\log(L_{\text{bol}}/[\text{erg s}^{-1}]) = 45.4-46.5$).

Most of the ALMA targets have relatively high hydrogen column densities ($\log(N_{\text{H}}/\text{cm}^{-2}) = 23.1-24.3$), with the exception of X_N_81_44, which has an upper limit ($\log(N_{\text{H}}/\text{cm}^{-2}) < 21.9$). The three ALMA targets with the lowest N_{H} are classified as optical broad line (Type 1) AGN. Our ALMA sample includes 7/8 (88%) obscured sources (based on $\log(N_{\text{H}}/\text{cm}^{-2}) > 22$; [Mainieri et al. 2002](#); [Szokoly et al. 2004](#)), compared to 54% in the parent sample, and 5/8 (63%) optical Type 2 (narrow line) AGN, compared to 41% in the parent sample. However, if we consider only SUPER targets with photometric coverage in the FIR, 18/26 (70%) have $\log N_{\text{H}}/\text{cm}^{-2} > 22$ and 15/26 (58%) are classified as optical Type 2 AGN. The targets with FIR observations are biased against unobscured (Type 1) AGN. This is due to the fact that Type 1 targets in SUPER are mostly located in the XMM-XXL, WISSH and Stripe82X fields, which do not have a good FIR coverage: WISSH and Stripe82X do not have FIR photometric observations available and XMM-XXL has FIR coverage for only some of the targets. On the contrary, the CDF-S and COSMOS fields have good FIR coverage, and the SUPER targets in those fields are biased towards Type 2 objects (73% of the objects, compared to 41% in the total SUPER sample) which is expected given that these two fields have the deepest X-ray observations (e.g. [Mainieri et al. 2002](#)). We conclude that the high N_{H} values of our sample are likely due to the fact that obscured targets are preferentially located in the two fields (COSMOS and CDF-S) with good FIR photometry.

In summary, although the ALMA sample presented in this paper has bolometric luminosities which are representative of the parent sample, we are biased towards heavily obscured (high N_{H}) and Type 2 targets. We discuss how representative our ALMA sample is in terms of SFRs and stellar masses in Sect. 3.4.

² AGN bolometric luminosities are derived from the fit of the multi-wavelength spectral energy distributions (SEDs) (for details, see [Circosta et al. 2018](#)).

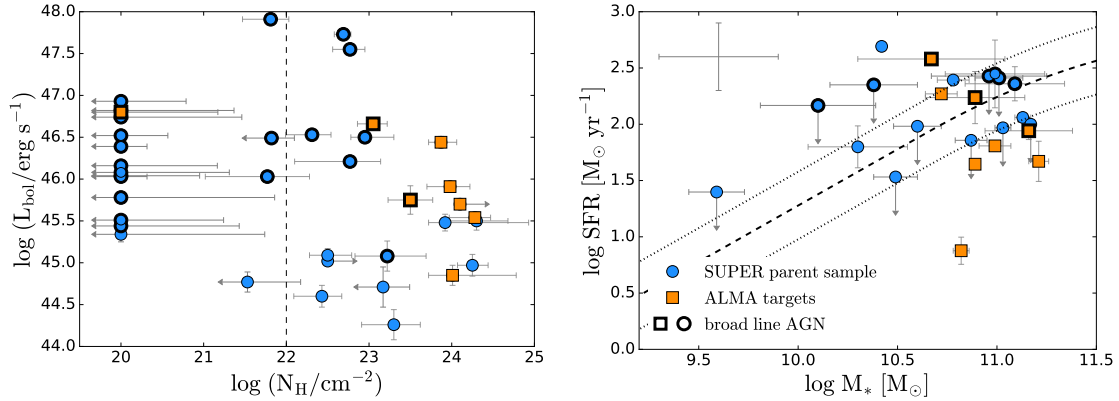


Fig. 1. *Left:* AGN bolometric luminosity versus hydrogen column density (N_{H}) for the SUPER sample. ALMA targets from this work are marked with orange squares. Targets classified as broad line AGN in the optical are marked with black contours. The dashed line at $\log(N_{\text{H}}/\text{cm}^{-2}) = 22$ marks the separation between X-ray unobscured and obscured AGN. *Right:* SUPER sample in the star formation rate (SFR) vs. stellar mass (M_{*}) plane. Only the 24/39 objects with SFR and stellar mass constraints are shown. The size of the systematic uncertainties is shown on the top left corner. The black dashed curve shows the main sequence (MS) of star-forming galaxies from Schreiber et al. (2015) at the average redshift of our target sample ($z \sim 2.3$), the 0.3 dex dispersion is shown by dotted lines. Most of the ALMA targets are consistent with being on the MS, with the exception of cid_1143, which lies below.

3. ALMA observations and analyses

We use FIR continuum observations from ALMA with the goal of tracing the dust obscured star formation at the same resolution (~ 2 kpc) as the [O III] and $H\alpha$ emission line maps extracted from our SINFONI IFS data. The ALMA Band 7 continuum observations used in this work belong to the Cycle 6 observing programme ID 2018.1.00992.S (P.I: C. M. Harrison).

Observations were taken between 18 October and 5 November 2018. The on-source integration time for each target is between 14 and 70 min. The observations were performed with 45–49 antennas, with baselines in the range 15.1–2500 m. The Band 7 870 μm continuum observations correspond to rest-frame 250–277 μm for our sources. The requested angular resolution was 0.15–0.30'', to match the resolution of the SINFONI observations. The maximum recoverable scales are in the range 1.9–2.8''. The field of view is $\sim 17''$.

3.1. Data reduction and imaging

We reduced the data using the Common Astronomy Software Application (CASA) version 5.4.0. The calibrated measurement sets were created using the standard ALMA pipeline provided with the raw data in the ALMA archive. We used the CASA task `fixvis` to phase-centre the calibrated measurement set on the central position of the source, determined by fitting a 2D Gaussian profile on the reduced image provided by the ALMA data-reduction pipeline.

We produced an image of the calibrated measurement set using the CASA task `tclean`. We measured the root mean square (rms) noise from the dirty image (obtained without applying the primary-beam correction), excluding the emission from the sources. We set the cleaning threshold of `tclean` to $2 \times \text{rms}$ and the pixel size to be one fifth of the beam size. In three cases (cid_451, cid_1205 and cid_1143), there is a secondary source in the field of view. The secondary sources are at a distance of $\sim 2.5''$, $8''$ and $9''$ from the primary target for cid_1205, cid_451 and cid_1143, respectively. We modelled the secondary source with a 2D Gaussian and then we removed it from the uv -data using the CASA task `uvsub`. We note that in all cases the presence of the secondary source does not affect significantly our

size measurements. We also tested that fitting the two sources simultaneously in the uv -plane gives consistent results.

One of our aims is to compare location, sizes and morphologies between the FIR emission, measured from the ALMA maps, and the ionised gas emission, measured with SINFONI. Thus, we want to create ALMA maps with a similar resolution to the SINFONI IFS maps (FWHM PSF $\sim 0.3''$). We generated the maps using the Briggs weighting scheme with robust parameter = 2 (corresponding to natural weighting). The beam sizes obtained using natural weighting are in the range 0.17–0.25'' and closely match the resolution of the SINFONI maps. We also created maps using the Briggs weighting scheme with robust = 0.5 (higher resolution, beam size 0.16–0.20'') and we found no appreciable difference in the morphology and size of the FIR emission that would affect our conclusions. Therefore we decided to use the maps obtained with natural weighting for the rest of the analysis. We show these final ALMA maps in Fig. 2.

We re-measured the rms from the ‘clean’ maps produced with natural weighting. The rms are in the range 15–31 $\mu\text{Jy beam}^{-1}$. We measured the peak signal-to-noise ratio (S/N) of the sources by dividing the peak flux density by the rms. The S/N values vary between 3.6 and 29. Two of the targets (cid_1057 and cid_451) have low S/N ($\ll 10$), and therefore we cannot derive reliable size measurements for these objects (Simpson et al. 2015). We highlight these two targets with low S/N in all the relevant figures. The beam size, rms, and peak signal-to-noise of the ALMA images are summarised in Table 2.

3.2. Modelling the ALMA continuum data: sizes and flux densities

In this section, we describe how we measure the sizes and flux densities of the 260 μm (rest-frame) emission. In particular, we are interested in comparing the 260 μm sizes with FIR sizes of literature samples, to test whether AGN show different sizes compared to non-AGN. We also want to compare the FIR sizes with the sizes of the optical emission-line regions ($H\alpha$ and [O III]), to investigate whether they are tracing similar spatial scales.

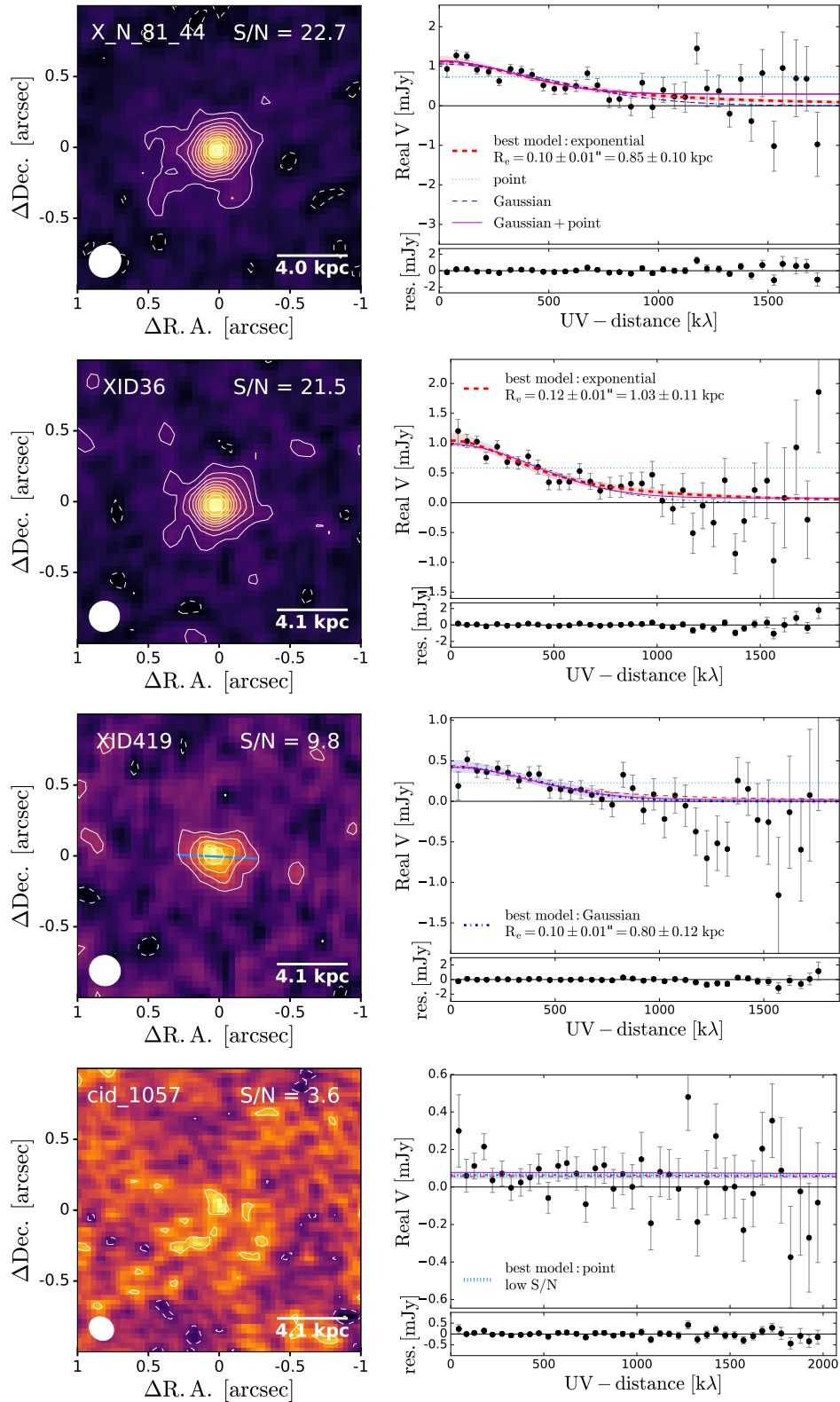


Fig. 2. *Left column:* maps of the ALMA continuum. The white ellipse represents the ALMA beam. The peak S/N is also shown. Contours start at 2σ and increase at intervals of 2σ . Dashed contours are negative contours at -2σ . The lightblue line indicates the position angle along the major axis of the FIR emission, when it can be reliably determined (see Sect. 3.3.1). *Right column:* real part of the visibilities versus uv -distance. The overlaid straight and curved lines show the fit using different models: point source (dotted lightblue line), exponential (dashed red curve), Gaussian (dashed-dotted blue curve), and Gaussian profile plus point source (solid magenta curve). The best model according the Bayesian Information Criterion (BIC) is labelled in each case. The shaded area shows the 1σ uncertainties on the best fit model. *Lower panel:* residuals with respect to the best-fit model.

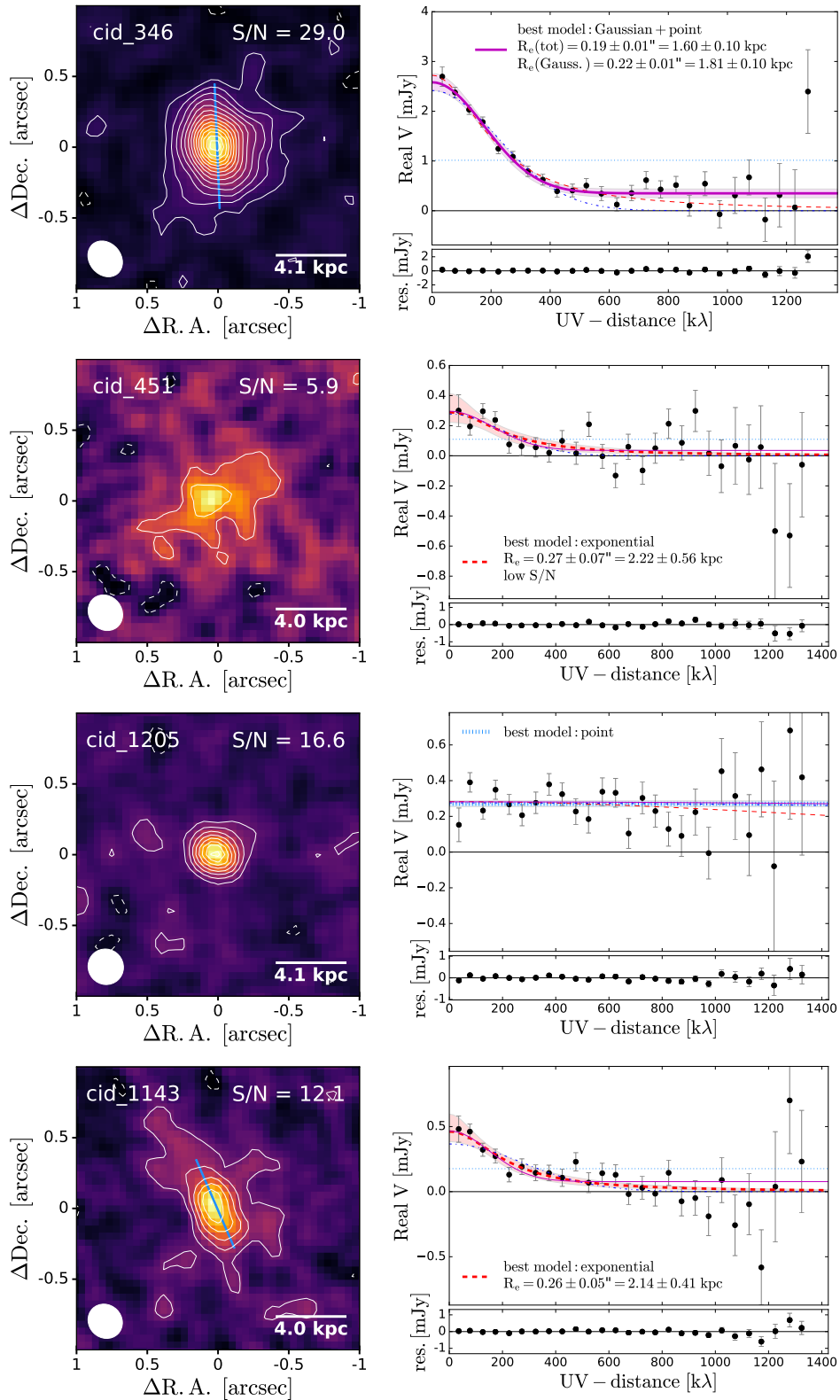


Fig. 2. continued.

We tested models describing different morphologies (e.g. point source, exponential disk profile) to extract reliable size and flux density measurements. We measured the sizes both from the visibilities and in the image plane. Measuring the sizes directly from the uv -visibilities has the advantage that it is not dependent on the choices made to create the images (e.g. weighting scheme,

cleaning threshold, ...). For completeness, all of the size measurements using the different methods are shown in Tables B.1 and B.2.

First we used the CASA routine `uvmodelfit` to fit a model directly to the visibilities. The models available with `uvmodelfit` are a point source, a 2D Gaussian and an elliptical

Table 2. Properties of the ALMA maps and measurement of FIR sizes and flux densities at rest-frame $\sim 260 \mu\text{m}$.

ID	Beam size [arcsec ²] (1)	rms [$\mu\text{Jy beam}^{-1}$] (2)	S/N (3)	Best model (4)	F(260 μm) [mJy] (5)	R_e [arcsec] (6)	R_e [kpc] (7)	Axial ratio (8)	PA [deg.] (9)	f_{AGN} % (10)	f_{sync} % (11)	α_r (12)
X_N_81_44	0.23 \times 0.22	31.44	22.7	Exponential	1.13 \pm 0.16	0.10 \pm 0.01	0.83 \pm 0.10	1.00 \pm 0.11*	–	<1	<1	–0.70
XID36	0.22 \times 0.21	26.62	21.5	Exponential	1.05 \pm 0.13	0.12 \pm 0.01	1.00 \pm 0.10	1.22 \pm 0.12*	–	3	<1	–1.25
XID419	0.22 \times 0.21	23.49	9.8	Gaussian	0.43 \pm 0.05	0.10 \pm 0.01	0.79 \pm 0.12	2.9 \pm 0.8	88 \pm 5	4	<1	–0.70
cid_1057	0.18 \times 0.16	16.34	3.6 ^(*)	Point	0.06 \pm 0.02	–	–	–	–	3	<1	–0.70
cid_346	0.27 \times 0.22	31.40	29.0	Gauss.+point	2.58 \pm 0.14	0.19 \pm 0.01	1.61 \pm 0.09	1.3 \pm 0.1	2 \pm 5	<1	<1	–0.98
cid_451	0.26 \times 0.23	16.25	5.9 ^(*)	Exponential	0.29 \pm 0.09	0.24 \pm 0.07	1.98 \pm 0.55	3.1 \pm 0.8	–58 \pm 5	6	21	–0.99
cid_1205	0.25 \times 0.25	16.20	16.6	Point	0.27 \pm 0.02	<0.12	<2.06	–	–	<1	<1	–0.70
cid_1143	0.25 \times 0.23	14.76	12.1	Exponential	0.46 \pm 0.11	0.25 \pm 0.05	2.01 \pm 0.41	4.6 \pm 0.7	23 \pm 2	<1	<1	–0.70

Notes. (1) Synthesized beam size (FWHM) of the ALMA maps created with Briggs weighting with robust = 2. (2) rms noise (measured from the ‘clean’ maps). (3) Peak signal-to-noise in the ALMA map. (4) Best fit model to the uv -visibility data, according to the Bayesian Information Criterion (BIC). ^(*)If the peak $S/N < 8$ in the ALMA maps, we do not consider the size measurements to be reliable. (5) Flux density at rest-frame $\sim 260 \mu\text{m}$, measured from the uv -visibilities using the best model. (6) Half-light radius (deconvolved from the beam) in arcsec measured from the uv -visibilities using the best model. For cid_1057 the radius is not reported due to the low S/N . (7) Half-light radius in kpc. (8) Axial ratio measured using `uvmodelfit` (excluding point sources). Axial ratios consistent with one are marked with *. (9) Position angle (PA) measured using `uvmodelfit` for the objects with axial ratios significantly different from one. The PA measures the angle of the major axis with respect to the north in anti-clockwise direction. (10) AGN contribution to the rest-frame 260 μm ALMA flux, estimated from the SED fit. (11) Contribution from synchrotron emission to the rest-frame 260 μm ALMA flux. We model the synchrotron emission as a power law with a spectral index α_r . (12) Spectral index α_r used to estimate the synchrotron contribution, calculated from the 1.4, 3 and 5.5 GHz data (when available). In the cases where we could not constrain α_r with the available data, we assume $\alpha_r = -0.7$ (see Sect. 5.1).

disk. We ran `uvmodelfit` on the phase-centred calibrated measurement sets assuming a 2D Gaussian model and using 20 iterations, which are enough to reach convergence. We note that `uvmodelfit` measures the intrinsic sizes, deconvolved from the beam. The results from `uvmodelfit` also provide the information on the ratio of the major and minor axis (see Table 2).

We also performed a fit on the collapsed visibilities using python outside of CASA, which gives us more freedom in the choice of models. We extracted the visibility amplitudes from the phase-centred calibrated measurements sets. Then, we binned the data in uv -distance intervals of 50 $k\lambda$. We measured the average of the visibilities at each uv -distance, weighted by the corresponding uncertainties. The uncertainty on each mean visibility is given by the standard deviation of the mean divided by the square root of the number of visibility points in that bin. In Fig. 2 we show the visibility amplitudes as a function of uv -distance for our sample.

For simplicity, we only considered symmetrical models, that is an axial ratio of one. We note that the radii derived with symmetrical Gaussian models are consistent with the mean radii measured with `uvmodelfit`. We tested the following models: point source, 2D Gaussian, 2D Gaussian plus a point source, and exponential profile (equivalent to a Sérsic profile with index $n = 1$).

To fit the visibilities versus uv -distances, we used the Markov chain Monte Carlo (MCMC) program Stan³ (Carpenter et al. 2017), which allows us to accurately estimate the uncertainties on the derived parameters. Specifically, we employed PyStan⁴, the python interface to Stan. We assumed a Gaussian likelihood and use uniform priors, allowing the free parameters to vary in a large parameter range (the prior ranges are tabulated in Table A.1).

We derived the best fit parameters by taking the median values from the marginal posterior distributions. The uncertainties are given as the 16th and 84th percentiles of the posterior distributions. We express all sizes in terms of half-light radius (also known as effective radius) R_e . For a 2D Gaussian, R_e is

equivalent to $0.5 \times FWHM$. For the exponential profile $I(R) = \exp(-R/a)$, where a is the scale parameter, R_e is given by $1.6783 \times a$. For the model with Gaussian plus point source, we calculate the radius that contains half of the light based on the total profile derived from the fit, $R_e(\text{tot})$. We also report the value of R_e for the Gaussian component only, $R_e(\text{Gauss.})$.

The results from our fit on the visibilities using a Gaussian model are consistent within the uncertainties with the results from `uvmodelfit` both in terms of sizes and flux densities. Therefore, for the rest of this work we use the flux densities and size measurements from our analysis of the collapsed visibility amplitude versus uv -distance performed in python.

To assess the preferred model to fit our data, we use the Bayesian Information Criterion (BIC; Schwarz 1978):

$$\text{BIC} = -2 \cdot \ln L + q \cdot \ln(m), \quad (1)$$

where L is the likelihood (i.e. the probability of the data given the parameters), q is the number of free parameters of the model, and m is the number of data points. The BIC considers the likelihood of the model and penalises models with a larger number of parameters. The model with the smallest BIC is the preferred model⁵. Figure 2 shows the visibilities versus uv -distances data with the curves showing the different models fitted. The preferred model is highlighted with a thicker line.

At least a $S/N \gtrsim 10$ on the flux is required to obtain reliable size measurements (Simpson et al. 2015). XID419 has $S/N = 9.8$ and is therefore a borderline case. Given the good agreement in the size measured with different methods for this source, we consider the size measurements to be reliable. cid_1057 and cid_451 have very low S/N (3.6 and 5.9, respectively), therefore we do not consider the size measurements of these two targets to be reliable. However, for completeness we show their values throughout the figures, and we highlight them as unreliable. For these two sources, the flux densities measured from the uv -visibilities are more uncertain. Thus, we also check the

⁵ We note that using the Akaike Information Criterion (AIC) or the Akaike Information Criterion corrected for sample size (Akaike 1973, 1974) will give the same qualitative results.

³ <http://mc-stan.org/>

⁴ <https://pystan.readthedocs.io/en/latest/>

flux densities derived from the ALMA images created by applying tapering (with tapering size = 0.5'') using CASA. The peak flux densities measured in the tapered images are in agreement (within the uncertainties) with the ones measured from the fit of the *uv*-visibilities.

We verify that we obtain consistent results by performing the analysis also in the image plane, using the 2D Gaussian fitting routine available in the CASA viewer. The sizes and flux densities measured in the image plane are in agreement with the measurements done in the *uv*-plane using the Gaussian model. For more details on the comparison between different methods, see Appendix B.

The sizes and flux densities measured with the different methods are reported in Tables B.1 and B.2. The measurements done in the image plane, with `uvmodelfit`, and fitting the *uv*-visibilities with the ‘preferred model’ are in general agreement (see Fig. B.1). We consider as our ‘best measurements’ the FIR sizes and flux densities derived from the fit of the *uv*-visibilities with the ‘preferred model’ (reported in Table 2). Given the general agreement between the different methods, the choice of the method does not affect our results. Nevertheless, we provide the information on the sizes measured with the different methods to ease the comparison with literature values (see Sect. 5.2).

3.3. FIR sizes, morphologies, and flux densities

3.3.1. FIR sizes and morphologies

The effective radii derived from the ‘best fit’ models for our sample are in the range 0.80–2.13 kpc, with a median of 1.31 ± 0.23 kpc⁶. The sizes measured from the fit with an exponential profile are larger than the sizes derived assuming a Gaussian profile by a factor of 1.38 on average (for the extended sources). This is by construction, since the exponential profile decreases less rapidly toward zero at larger radii than the Gaussian profile and therefore there is a larger fraction of flux at large distances. However, we note that our conclusions do not change if we choose one of these models for all sources. To facilitate comparison with literature values (where both these models are considered), we provide the results from both models in Appendix B.

Half of the sources with reliable size measurements (3/6) are best described by an exponential profile according to the BIC. One source (cid_1205) is better described by a point source and one source (XID419) by a Gaussian. The preferred model for cid_346 is a Gaussian plus a point source. The point source accounts for 13.5% of the total flux density, according to the results of our fit. For this source, we also test a model consisting of an exponential profile plus a point source. This model gives a point source contribution to the total flux of 4.1%, but it is not preferred over the ‘Gaussian plus point source’ or the ‘exponential profile’ model, according to the BIC. The point source component could be either due to the emission from a compact starburst or from the AGN. From our SED fitting decomposition, the AGN component contributes only 0.15% to the total 260 μ m flux density, thus it cannot account for all the flux of the observed point source. Therefore, a compact star-forming region may be a more likely scenario. Since we have only two objects which require a point source in the model, and in the case of cid_346 its contribution to the total flux is marginal, we consider this as an indication that on average point source emission from AGN

heated dust at this wavelength is not prominent (see Sect. 5.1 for further discussion on the origin of the FIR emission).

The ratios between the major and minor axis derived using `uvmodelfit` for the 6/8 sources with high S/N are in the range 1–4.6. For two sources (X_N_81_44 and cid_1205) the axial ratio is consistent with one. For XID_419, cid_346, and cid_1143 the difference in the sizes of the major and minor axes show that the emission is significantly elongated in one direction (axial ratio >1.3). For these three sources, we report also the position angle measured with `uvmodelfit` (see Table 2).

3.3.2. Flux densities

The flux densities measured with the different methods are in agreement within the uncertainties (see Fig. B.1). The only exception is cid_346, for which the `uvmodelfit` Gaussian fit gives a slightly smaller flux (8%) than the other methods. This is probably because the Gaussian model cannot well describe the point source emission in the centre, and therefore misses part of the flux.

Our high-resolution ALMA images are potentially missing some of the more diffuse emission, and therefore the measured flux densities cannot be considered as ‘total’ flux densities. For example, Harrison et al. (2016a) found a drop in peak flux of 18–44% between a resolution of 0.8'' and 0.3''. To assess how much flux we are potentially missing in our ALMA data, we compare these flux measurements with other 260 μ m flux measurements from lower resolution data from the ALMA Archive (compiled by Circosta et al. 2018) and from Scholtz et al. (2020). Three sources have 260 μ m fluxes from lower resolution data. XID419 has an upper limit from Scholtz et al. (2020), that is consistent with our measurement. For cid_451 and cid_1205, our flux density measurements are consistent within the uncertainties with the 260 μ m flux densities from the low-resolution data. Therefore, there is no evidence that the ALMA images are resolving out a large portion of the flux.

3.4. SED fits including the ALMA flux densities

In this section, we fit the spectral energy distributions (SEDs) of our targets to estimate the stellar masses and SFRs of their host galaxies. We used the UV-FIR photometric catalogue from Circosta et al. (2018) and we added the ALMA band-7 flux densities. Given the large number of upper limits and the large point spread function (PSF) of the *Herschel* images, including the ALMA fluxes helps to place better constraints on the properties of the host galaxies. Moreover, in Sect. 5.1 we use these best-fit SED models to estimate the AGN contribution to the ~ 260 μ m flux densities.

In addition to including the ALMA photometry, we took a conservative approach for the weakly detected or possibly contaminated *Herschel* sources; specifically, we considered the *Herschel* fluxes as upper limits for X_N_81_44, cid_1057, cid_1205 and cid_1143. However, if we use the full photometry catalogue used in Circosta et al. (2018), even excluding the ALMA Band 7 photometry, we reach the same conclusions in terms of AGN contributions (see Sect. 5.1).

We use the same SED fitting approach used by Circosta et al. (2018) for the full SUPER sample, with the only difference that we include the ALMA band 7 photometry. Circosta et al. (2018) performed the panchromatic (UV-to-FIR) SED fitting using the Code Investigating GALaxy Emission (CIGALE; Burgarella et al. 2005; Noll et al. 2009; Boquien et al. 2019). This code takes into account the energy balance between the absorption by dust in

⁶ The error on the median is calculated as the standard deviation of the measurements divided by the square root of the number of objects.

the UV-optical and the corresponding re-emission in the FIR. The SED model includes three emission components: (i) stellar emission; (ii) emission by cold dust heated by star formation; (iii) AGN emission, consisting in direct emission from the accretion disk in the UV-optical range and emission from the dusty torus peaking in the mid-infrared (MIR). For more details on the SED fitting method we refer the reader to [Circosta et al. \(2018\)](#).

The SFRs are estimated from the infra-red (IR) luminosity, obtained by integrating the best-fit template SED in the rest-frame wavelength range 8–1000 μm , after removing the AGN contribution. The IR luminosity is converted to SFR using the [Kennicutt \(1998\)](#) calibration, converted from a Salpeter IMF to a [Chabrier \(2003\)](#) IMF by subtracting 0.23 dex ([Bolzonella et al. 2010](#))⁷. Figure E.1 shows the SEDs with the results from the SED fitting and the measured ALMA 260 μm flux densities. The SFR and stellar masses derived from these SED fits are reported in Table 1.

We compare the SFR and stellar masses derived from the SED including the ALMA data with the values reported in [Circosta et al. \(2018\)](#). The SFRs vary by less than 0.13 dex for all targets except for cid_1205 (−0.6 dex) and cid_1143 (−1.2 dex). The large difference for cid_1143 can be explained by the fact that the *Herschel* fluxes are all upper limits, thus the previous SFR needs to be considered as an upper limit. For cid_1205, the *Herschel* fluxes used to calculate the previous SFR value included also the flux from the companion galaxy, thus the previous SFR was an upper limit. For cid_451, only an upper limit on the SFR ($<125 M_{\odot} \text{yr}^{-1}$) was reported in [Circosta et al. \(2018\)](#) due to the possible high contamination from synchrotron emission to the FIR fluxes. This target is classified as a radio-loud source based on the comparison between infrared and radio luminosity. We take advantage of the ALMA Band 3 flux measurement at rest-frame 1 mm recently presented in [Circosta et al. \(2021\)](#) to better constrain the contribution from the AGN synchrotron emission to the FIR fluxes (see Sect. 5.1). We re-measure the SFR after subtracting the synchrotron contribution from the FIR fluxes and obtain $\text{SFR} = 48 \pm 19 M_{\odot} \text{yr}^{-1}$. The stellar masses differences with respect to the previous measurements are ≤ 0.42 dex (mean 0.14 dex). cid_1143 shows the largest difference in stellar mass.

The right panel of Fig. 1 shows the parent SUPER sample and the subset targeted for ALMA observations in this work on the SFR versus stellar mass (M_*) plane. The ALMA targets have stellar masses in the range $\log(M_*/M_{\odot}) = 10.7\text{--}11.2$, with a median $\log(M_*/M_{\odot}) = 10.9$. The SUPER parent sample has the same median $\log M_*/M_{\odot} = 10.9$, and an interquartile range $\log(M_*/M_{\odot}) = 10.6\text{--}11.0$. The SFRs of the ALMA sample are in the range $\text{SFR} = 8\text{--}380 M_{\odot} \text{yr}^{-1}$, with a median $\text{SFR} = 76 M_{\odot} \text{yr}^{-1}$. The SUPER parent sample has a median $\text{SFR} = 144 M_{\odot} \text{yr}^{-1}$ and interquartile range $\text{SFR} = 63\text{--}242 M_{\odot} \text{yr}^{-1}$. The ALMA targets have similar stellar masses and (slightly lower) SFRs to the objects with SFR and stellar mass measurements in the parent SUPER sample. However, we note that only 24/39 of the SUPER targets have SFR and stellar mass measurements, and ten of these have only upper limits on the SFR, which are not taken into account in the above median and interquartile ranges. Given the presence of many SFR upper limits in the parent sample, our targets are likely to

represent the upper end of the SFR distribution of the SUPER sample.

On the SFR– M_* plane (see Fig. 1), we show also the main-sequence definition by [Schreiber et al. \(2015\)](#) at the average redshift of our sample ($z \sim 2.3$). Most of the ALMA targets lie on the main-sequence or slightly below⁸. The exception is cid_1143, which lies clearly below the main-sequence. Despite the pre-selection of FIR detections, our ALMA targets are mainly main-sequence galaxies. However, SUPER primarily consists of moderate luminosity X-ray AGN which, as a population, tend to have SFR distributions slightly below the main-sequence (e.g. [Mullaney et al. 2015](#); [Scholtz et al. 2018](#); [Grimmett et al. 2020](#)). [Scholtz et al. \(2018\)](#) study the specific SFR ($\text{SSFR} = \text{SFR}/M_*$) distribution of a sample of 81 AGN at $z = 1.5\text{--}3.2$ and for AGN with X-ray luminosities $L_{2\text{--}10\text{keV}} > 10^{44} \text{erg s}^{-1}$, they measure the mode of the SSFR distribution $\log(\text{SSFR}/\text{Gyr}^{-1}) = -0.32 \pm 0.16$. For the SUPER targets with SFR and stellar mass measurements, the mean is $\log(\text{SSFR}/\text{Gyr}^{-1}) = 0.19 \pm 0.09$. Thus, the SUPER sample is likely to have a distribution of SFRs skewed to higher values compared with the parent population of X-ray AGN.

4. H α and [OIII] observations and analysis

4.1. SINFONI observations and data reduction

The SINFONI Adaptive Optics (AO) assisted observations and data reduction are described in detail in [Kakkad et al. \(2020\)](#), for the Type 1s, and in Perna et al. (in prep.), for the Type 2s. Here we summarise the main information. The SINFONI observations took place between November 2015 and December 2018 (ESO large program 196.A-0377). We observe the *H*-band (1.45–1.85 μm), which includes the rest frame optical lines $H\beta$ and [O III] $\lambda\lambda 4959, 5007$, and the *K*-band (1.95–2.45 μm), which includes the [N II] $\lambda\lambda 6584, 6548$, $H\alpha$ and [S II] $\lambda\lambda 6716, 6731$ lines. The average spectral resolution in the *H*-band and *K*-band is ~ 3000 and ~ 4000 respectively, corresponding to a channel width of $\sim 2 \text{\AA}$ and $\sim 2.5 \text{\AA}$, respectively. The PSF sizes of the *H*-band and *K*-band are in the range 0.27–0.52'' and 0.15–0.46'', respectively (the PSF sizes for each target are listed in Table 3). We note that cid_1057 is not detected in $H\alpha$, thus for this target we only show the [O III] (i.e. *H*-band) data.

4.2. Astrometry registration

Since one of our main goals is to compare the spatial distribution of the FIR continuum and ionised gas emission, we need to have reliable astrometry for both ALMA and the SINFONI maps. The absolute position of the SINFONI cubes, as derived from the SINFONI pipeline, is not sufficiently accurate for our purposes. Given the small field of view of the SINFONI images ($3 \times 3 \text{arcsec}^2$), we cannot correct the astrometry using nearby stars, since usually the target is the only visible source in the field of view. Thus, we need to rely on coordinates derived from other images.

We aligned our SINFONI data-cubes to broadband *H*- and *K*-band images of the same field. We used images from VLT/VISTA taken as part of the UltraVISTA survey for

⁷ Systematic uncertainties on the stellar masses are around 0.3 dex and can be larger for SFRs (e.g. [Mancini et al. 2011](#); [Santini et al. 2015](#)). These uncertainties are due to the models used, degeneracies between parameters, a priori assumptions and the discrete coverage of the parameter space.

⁸ We note that the main-sequence from [Schreiber et al. \(2015\)](#) is derived assuming a Salpeter IMF ([Salpeter 1955](#)), while we assume a Chabrier IMF ([Chabrier 2003](#)). However, assuming a different IMF would systematically shift both M_* and SFRs by approximately the same amount ([Brinchmann et al. 2004](#); [Elbaz et al. 2007](#)), and therefore would not affect the shape of the main-sequence.

Table 3. Information about the SINFONI maps.

ID	<i>H</i> -band PSF [arcsec ²]	<i>K</i> -band PSF [arcsec ²]	$z_{[\text{O III}]}$	F([O III])/F(H β)	F([N II])/F(H α)	R_e ([O III]) [kpc]	R_e (H α) [kpc]	Line components
(1)	(2)	(3)	(4)	(5)	(6)	(7)	(8)	(9)
X_N_81_44	0.27 × 0.27	0.24 × 0.24	2.3180	>8.00	<0.10	<1.11	3.48 ± 0.08	n, b, BLR
XID36	0.35 × 0.35	0.15 × 0.15	2.2578	10.15 ± 0.63	0.69 ± 0.12	1.06 ± 0.01	1.57 ± 0.01	n, b
XID419	0.52 × 0.47	0.24 × 0.22	2.1430	>2.15	0.91 ± 0.05	<2.07	1.42 ± 0.02	n
cid_1057	0.32 × 0.30	0.46 × 0.43	2.2099	2.51 ± 0.17	–	1.36 ± 0.01	–	n, b
cid_346	0.30 × 0.30	0.30 × 0.30	2.2170	1.58 ± 0.20	0.43 ± 0.11	1.99 ± 0.03	2.28 ± 0.05	n, b, BLR
cid_451	0.30 × 0.28	0.28 × 0.27	2.4434	>10.59	0.61 ± 0.03	0.78 ± 0.00	0.67 ± 0.01	n, b
cid_1205	0.30 × 0.30	0.30 × 0.30	2.2555	>1.66	–	0.99 ± 0.02	1.33 ± 0.09	n, BLR
cid_1143	0.41 × 0.38	0.30 × 0.30	2.4418	6.91 ± 1.97	0.75 ± 0.09	<1.62	0.92 ± 0.02	n, b

Notes. PSF of the *H* and *K*-band SINFONI images and line fluxes measured from the integrated spectra. If the S/N of a line is smaller than 3, we report a 5σ upper limit. For cid_1057, the S/N of the *K*-band image is too low to derive any information about the H α and [N II] emission. (4) Redshift derived from the narrow component of the [O III] line. (5) Ratio of the fluxes of [O III] λ 5007 and H β narrow emission lines. For Type 1 AGN, this is the flux of the narrow component, i.e. the BLR component is not included. (6) Ratio of the fluxes of [N II] λ 6548 and H α narrow emission lines. For Type 1 AGN, this is the flux of the narrow component, i.e. the BLR component is not included. (7) Half-light radius (R_e) of the [O III] systemic emission ($[-300, 300]$ km s⁻¹ range), deconvolved from the PSF. If R_e is smaller than the PSF, we give the size of the PSF as an upper limit. (8) Half-light radius (R_e) of the H α systemic emission ($[-300, 300]$ km s⁻¹ range), deconvolved from the PSF. (9) Components used to fit the emission lines. ‘n’: narrow component, ‘b’: broad component (for the outflow), ‘BLR’: broad line region component.

COSMOS (McCracken et al. 2012) and as part of the VHS (VISTA Hemisphere Survey) for XMM-XXL (McMahon et al. 2013), and from VLT/ISAAC for CDF-S (Retzlaff et al. 2010). We first aligned the *H/K*-band images to *Gaia* astrometry (Gaia Collaboration 2016, 2018) using several stars across the fields. We then made broad-band images from the SINFONI data-cubes by collapsing them over the same wavelength range as the archival *H/K*-band images. We found the centroids of the images from the data-cubes and aligned these to the positions of the corresponding source in the near-infrared VLT/VISTA or VLT/ISAAC (*H/K*-band) images⁹. For the uncertainties on these positions, we combined in quadrature the uncertainties from: (1) the *Gaia* coordinates (<4 mas), (2) the alignment of the *H/K*-band images with *Gaia* (75–130 mas), (3) the PSF of the VLT/VISTA or VLT/ISAAC *K*-band images (3–40 mas), (4) the 2D Gaussian fit to determine the position of sources in the VLT images (1–49 mas), and (5) the centroid position of the collapsed data-cubes (~25 mas). This results in uncertainties on the astrometry in our SINFONI cubes of 0.03–0.14″, corresponding to 1–3 pixels¹⁰. More details about the coordinate registration are provided in the Appendix C. The ALMA astrometry has an absolute accuracy of 2% of the synthesized beam (ALMA Cycle 6 Technical Handbook¹¹), which corresponds to ~3–6 mas for our observations and it is small enough compared to the other uncertainties.

4.3. Spectral line fitting

We use the integrated spectra to derive emission line flux ratios and investigate the main source of ionisation in our objects. For this purpose, we measure the fluxes of the H β , [O III] λ 4959,5007, H α and the [N II] λ 6548,6583 emission lines. The integrated SINFONI spectra of the H α + [N II] and H β + [O III] spectral regions for our targets are shown in Fig. 3.

⁹ For two of the Type 1 sources (X_N_81_44 and cid_346) we use the more accurate *Gaia* position and for XID419 we use more accurate coordinates from HST/WFC3, see Appendix C.

¹⁰ The largest uncertainties are due to the lower resolution of the VLT/ISAAC *K*-band images for the CDF-S field.

¹¹ <https://almascience.eso.org/documents-and-tools/cycle6/alma-technical-handbook>

The spectra are extracted from a circular aperture centred on the targets. The diameter of the aperture was defined to include at least ~95% of the emission.

Up to three Gaussian components were used to fit each emission line. These are a narrow (systemic) component, a broad (outflow) component and a broad line region (BLR) component (only for the Hydrogen lines). The components used for each target are summarised in Table 3.

For the Type 1 AGN, the H β + [O III] and H α + [N II] spectral regions are fitted separately. The modelling of the H β + [O III] spectral region is described in details in Kakkad et al. (2020). The width and relative position of the systemic and outflow components of H β and [O III] are tied together. The broad outflow component is used in the fit only if its addition decreases the reduced χ^2 value of the overall model. Specifically, for the three Type 1 in our sample: this is not required for cid_1205 but is required for X_N_81_44 and cid_346¹². An additional Gaussian component is used to model the broad line region (BLR) component of H β for all Type 1 sources. For the H α + [N II] spectral region, we use the same number of Gaussian components as for [O III], and an additional Gaussian component to model the BLR component of H α . Additionally, we apply the following constraints (following Vietri et al. 2020): (i) the widths of the broad components of H α and [N II] are tied to the width of the broad component of [O III], allowing variation in the parameters within the measurement errors; (ii) the relative centroid locations of the narrow and broad components of H α and [N II] are tied to the ones measured with [O III]; (iii) the maximum width allowed for the narrow H α component is set by the width of the narrow [O III] component plus its measurement error. Finally, empirical Fe II templates from the literature are used to model the Fe II emission (Boroson & Green 1992; Veron-Cetty et al. 2004; Tsuzuki et al. 2006).

For the Type 2 sources, the fitting procedure is similar to the one used for the Type 1 AGN. The results of the emission

¹² We note that in Kakkad et al. (2020) the H β + [O III] emission lines were fitted with one component, while two components are required for the fit of the H α + [N II] emission lines (based on the reduced χ^2). In order to have consistent measurements for the four emission lines, we decide to use the fit with two components also for the H β + [O III] emission lines.

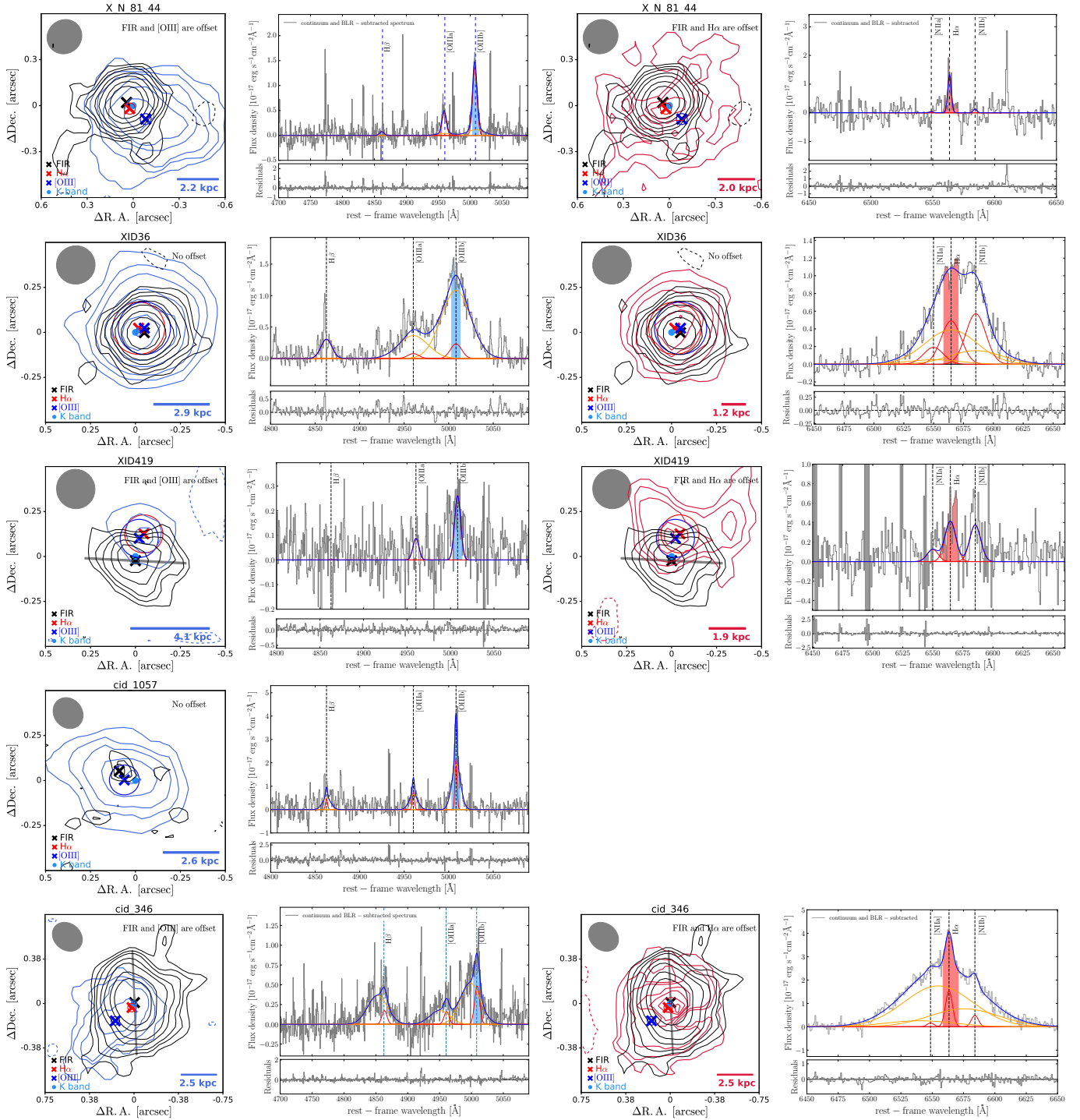


Fig. 3. [O III] and H α continuum-subtracted maps (where available), with the corresponding spectra. For the Type 1 AGN (X_N_81_44, cid_346 and cid_1205), the broad line region component is also subtracted. The [O III] and H α maps were created by integrating the spectrum over the $[-300, 300]$ km s $^{-1}$ velocity range, with respect to the centre of the line (see shaded regions on spectra). The [O III] and H α maps were created by integrating the spectrum over the $[-300, 300]$ km s $^{-1}$ velocity range, with respect to the centre of the line (see shaded regions on spectra). The FIR (black), [O III] (lightblue), and H α (red) emission contours are shown at the 2, 3, 4, 6, 8, 12, and 16 σ levels. Dashed lines indicate the negative -2σ contours. The crosses show the position of the centroid of the FIR (black), [O III] (blue) and H α (red) emission with the respective uncertainties (circles). The lightblue point shows the centroid position of the optical continuum (i.e. K-band observed-frame). In all maps, the grey ellipses show the size of the ALMA beam, while the scale-bars give the size of the PSF of the line emission maps. The grey bar shows the position angle along the major axis of the FIR emission, when it can be reliably determined (see Sect. 3.3.1). *Column 1:* contours of the [O III] emission (lightblue) and FIR (rest-frame) 260 μ m continuum emission (black). *Column 2:* continuum-subtracted (integrated) [O III]+H β spectra. The blue curve shows the total fit to the H β , [O III] λ 4959 and [O III] λ 5007 lines. The red and orange curves show the narrow and broad components. *Column 3:* contours of the narrow H α flux map (red) FIR (rest-frame) 260 μ m continuum emission (black). *Column 4:* same as Col. 2, but for the continuum-subtracted (integrated) H α + [N II] spectra. The blue curve shows the total fit to the H α , [N II] λ 6548 and [N II] λ 6584 lines.

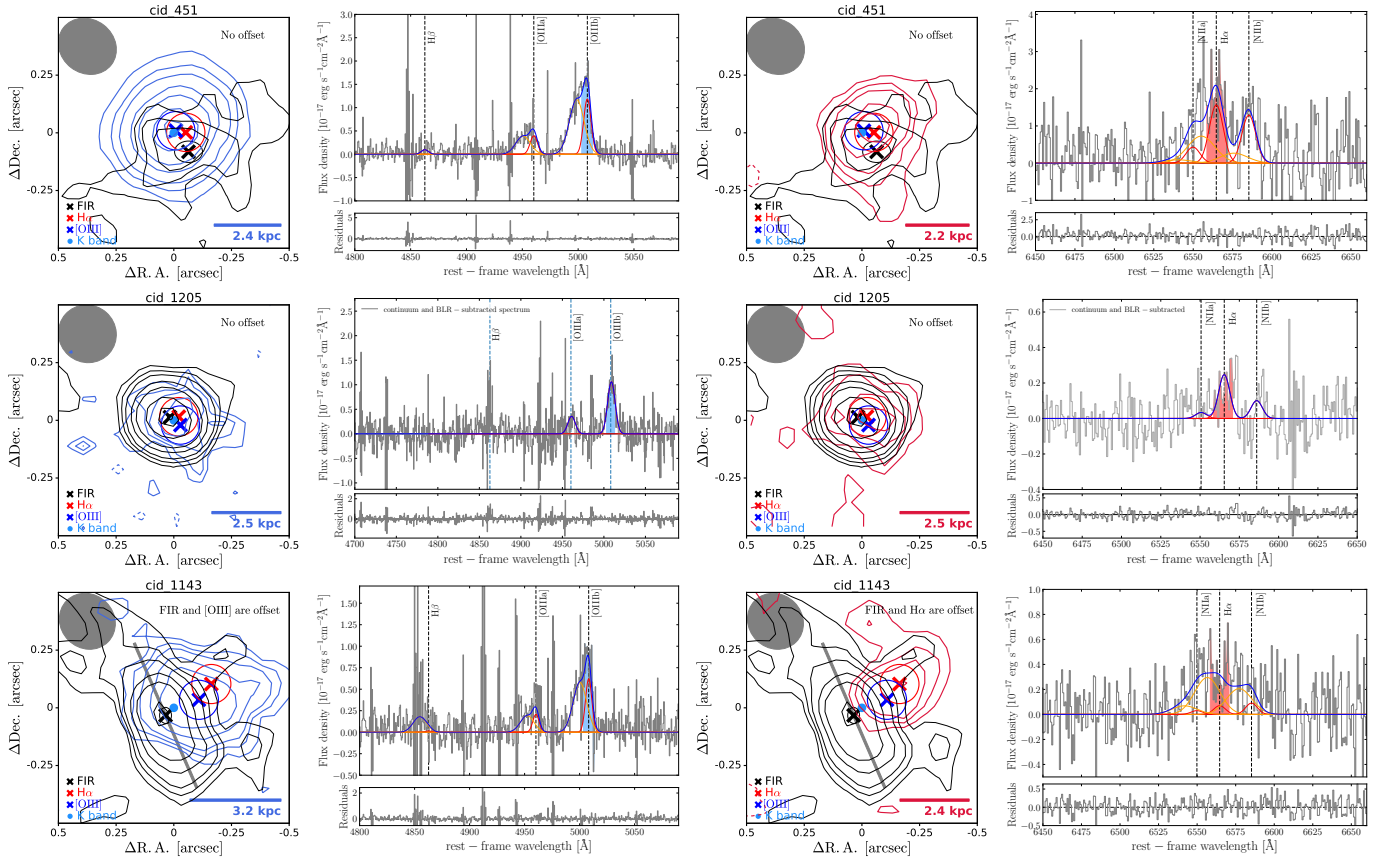


Fig. 3. continued.

line fits for all the Type 2 objects in the SUPER sample will be presented in Perna et al. (in prep.). The $H\alpha$ and $H\beta$ lines, and the [O III], [N II] and [S II] doublets were modelled using Gaussian profiles. The wavelength separation between emission lines was tied according to atomic physics, and the FWHM was constrained to be the same for all the emission lines. The relative flux of the two [N II] and [O III] lines was fixed to 2.99 (Osterbrock & Ferland 2006). Each spectral fit was performed with one and two Gaussian components (each centred at a given velocity and with a given FWHM). The Bayesian information criterion (BIC, Schwarz 1978) was used to decide whether a second component was needed for the fit (see e.g. Perna et al. 2019). All targets require a second component except for XID419. We note that we use our emission-line profile fits to characterise the integrated emission-line profiles; however, in this study we do not attempt to map individual $H\alpha$ components associated with star formation, AGN narrow line regions and/or outflows (see Sect. 4.4).

The H and K -band (continuum- and BLR-subtracted) spectra with the corresponding emission line fits are shown in Fig. 3. The total spectra of the Type 1 targets (before subtracting the continuum and BLR components) are shown in Appendix D. A summary of the line components used for each target is provided in Table 3.

For both Type 1 and Type 2 sources, the uncertainties on the line fluxes were estimated using a Monte Carlo approach (for details, see Kakkad et al. 2020). We define a line as detected if it has a $S/N = F/F_{\text{err}} \geq 3$. If a line is not detected, we calculate a conservative upper limit equal to the flux of a Gaussian emission line with amplitude five times the noise level (measured in a line-free region of the spectrum) and with the same

width as the other detected emission lines. The 5σ upper limit corresponds to a ‘false negative’ fraction of 2%, which is the probability that a source with ‘true’ flux higher than this upper limit is not detected.

We note that we did not correct the line fluxes for obscuration. In most of the cases we are not able to calculate the Balmer decrement, because the $H\beta$ line is not detected. Nevertheless, we do not consider this a major limitation since we are mainly interested in the ratio of emission lines close in wavelength, which therefore are negligibly affected by differential obscuration.

4.4. $H\alpha$ and [O III] maps

In this section we describe the methods used to derive the maps of the narrow $H\alpha$ (i.e. without Broad Line Region) and [O III] emission. In this paper, we consider a w_{80} (i.e. the width containing 80% of the line emission) value $>600 \text{ km s}^{-1}$ as a signature of an AGN-driven outflow (Kakkad et al. 2020). Following this definition, we consider as non-outflowing emission a velocity range of 600 km s^{-1} , centred on the peak of the [O III] (or $H\alpha$) emission line. For the two targets with a two component fit to the [O III] emission line, this definition covers the bulk of the narrower component and excludes the broader, blue-shifted component. We note that it is possible that the outflow component is contributing also in the central velocity channel ($v = [-300, 300] \text{ km s}^{-1}$), especially in the sources with a strong outflow component. We chose this definition because we prefer to adopt a consistent definition across all targets and for both emission lines ($H\alpha$ and [O III]). Moreover, a definition which is as independent as possible from the modelling of the emission

line profile is highly preferred. However, it is inevitable that the resulting $H\alpha$ maps of the Type 1s will depend on the method used to subtract the BLR component.

To create the maps, we use the continuum-subtracted data-cubes. For the $H\alpha$ maps, we also subtract the BLR component (for the Type 1) and the [N II] components. For X_N_81_44, we note that the broad component of $H\beta$ is much more prominent than the broad component detected in [O III] (see Fig. D.1). We suspect that this component is a residual component belonging to the BLR. This argument is supported by the fact that the spatial distribution of the $H\beta$ broad component is similar to the spatial location of the BLR. Therefore, for this object we consider the broad $H\beta$ and $H\alpha$ components as part of the BLR and we subtract them from the data-cube. We use the peak of the modelled [O III] λ 5007 line profile to derive the systemic redshift and set the zero velocity (see Sect. 4.3). We create the [O III] and $H\alpha$ maps by collapsing the spectra over the selected velocity channels for each spaxel.

We note that our approach to map the $H\alpha$ emission line is different from the method applied in other resolved studies of the $H\alpha$ emission of Type 1 AGN (e.g. Carniani et al. 2016), where the residuals of the fit (of their AGN-dominated components) were used to trace $H\alpha$ emission due to star formation. After subtracting the emission line fitting model from our data, we do not find any significant residual at the position of $H\alpha$, both in the maps and in the integrated spectra (see residual panels in Fig. 3). Thus, we cannot use this method to map the $H\alpha$ emission from star formation. We defer to a future work a detailed investigation of the spatially-resolved narrow $H\alpha$ emission distribution and kinematics for the few Type 1 sources where the S/N are sufficiently high for such analyses. In Sect. 5.3.1 we use emission line diagnostics to investigate the main mechanism responsible for the ionisation of $H\alpha$ (star formation or AGN) in our objects. However, due to the limited S/N of our observations, we cannot perform a BPT analysis in a spatially resolved manner.

Figure 3 shows the contours of the $H\alpha$ and [O III] emission in the central 600 km s^{-1} channels. For every map, we measure the size and the centroid (‘peak position’) of the emission by fitting a 2D Gaussian using the python package `scipy.optimize.curve_fit`. The $H\alpha$ and [O III] sizes are reported in Table 3. We use these measurements in Sect. 5.3.2, where we compare the sizes and positions of the $H\alpha$ and [O III] emissions with the location of the FIR emission. The uncertainties on the positions are calculated by adding in quadrature the uncertainties on the coordinates registration (see Sect. 4.2) and the uncertainties due to the 2D Gaussian fit (mean uncertainty $\sim 2 \text{ mas}$). The uncertainties on the position are in the range $0.04\text{--}0.15''$.

5. Results and discussion

In this section, we first investigate the origin of the (rest-frame) $260 \mu\text{m}$ emission in our targets, to assess the relative importance of the physical processes responsible for the FIR emission (Sect. 5.1). Then, we compare the FIR size of our sample with other AGN hosts and non-AGN galaxies at similar redshift from the literature, to test whether our sample has similar sizes to the general population of $z \sim 2$ galaxies (Sect. 5.2). Finally, we compare the spatial distribution of the FIR emission with the ionised gas distribution (Sect. 5.3), as well as with the position of the ionised outflows (Sect. 5.4).

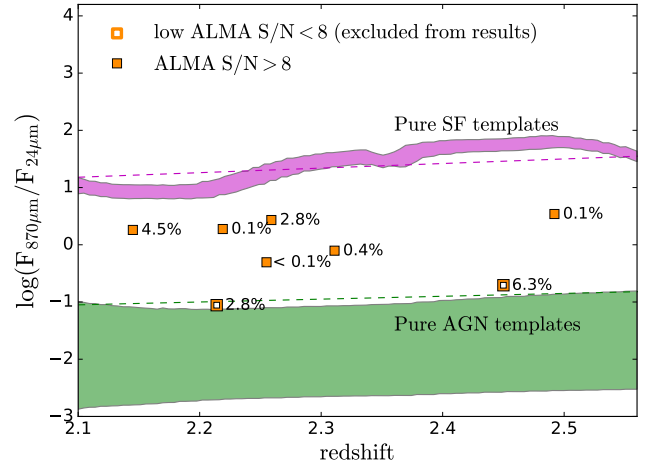


Fig. 4. Ratio of (observed-frame) $870 \mu\text{m}$ to $24 \mu\text{m}$ flux as a function of redshift for our targets calculated using the measured $F(870 \mu\text{m})$ from the ALMA maps. The two sources with peak $S/N < 8$ in the ALMA maps are marked with empty symbols (cid_1057 and cid_451). The numbers show the percentage AGN contribution at $870 \mu\text{m}$ (observed-frame) estimated from the modelled SEDs (see Sect. 5.1). The dashed lines show the median flux ratio as a function of redshift for star-forming (SF) galaxies templates (magenta) and AGN templates (green) from Stanley et al. (2018). The shaded areas show the range of flux ratios obtained from the SF (magenta) and AGN (green) templates used to fit our ALMA targets.

5.1. Origin of the FIR ALMA Band 7 emission

We compare the distribution of dust-obscured star formation with the distribution of ionised gas and corresponding ionised outflows in our targets. For this goal, we use the rest-frame FIR images from our ALMA $260 \mu\text{m}$ maps. However, it is important to first assess the physical processes that are responsible for the $260 \mu\text{m}$ emission in our sample, to test whether this emission can be used as a reliable tracer of dust obscured star formation.

The rest-frame $\sim 260 \mu\text{m}$ emission (corresponding to the observed $870 \mu\text{m}$ emission) can have different origins. The three main sources of emission in the FIR are: (1) dust heated by star formation, (2) dust heated by the AGN, and (3) AGN synchrotron emission (e.g. Falkendal et al. 2019). The observed emission is likely a combination of the three processes above, nevertheless in this section we attempt to estimate their fractional contribution, and to determine the dominant source of emission in our eight ALMA targets.

Dust heated by the AGN. We consider first a diagnostic to estimate the AGN contribution in the FIR that does not rely directly on our specific SED fits. Following Stanley et al. (2018), this method focuses on the ratio of the (observed-frame) FIR ($870 \mu\text{m}$) to MIR ($24 \mu\text{m}$) flux. AGN can have a stronger MIR emission compared to star-forming galaxies, due to emission from hot dust in the torus (e.g. Pier & Krolik 1992; Lacy et al. 2004; Donley et al. 2012; Stern et al. 2012). Therefore, looking at the (observed-frame) flux ratio $F_{870 \mu\text{m}}/F_{24 \mu\text{m}}$, it is possible to assess whether the SED is dominated by AGN emission in the $24\text{--}870 \mu\text{m}$ regime.

Figure 4 shows the $F_{870 \mu\text{m}}/F_{24 \mu\text{m}}$ flux ratios as a function of redshift for our sample. To compute the flux ratios, we use the $24 \mu\text{m}$ *Spitzer*/*MIPS* flux densities from the photometric catalogue compiled by Circosta et al. (2018) and our measurements of the $870 \mu\text{m}$ ALMA flux densities. On Fig. 4, we show the range of flux ratios obtained from the SED fit of our objects by

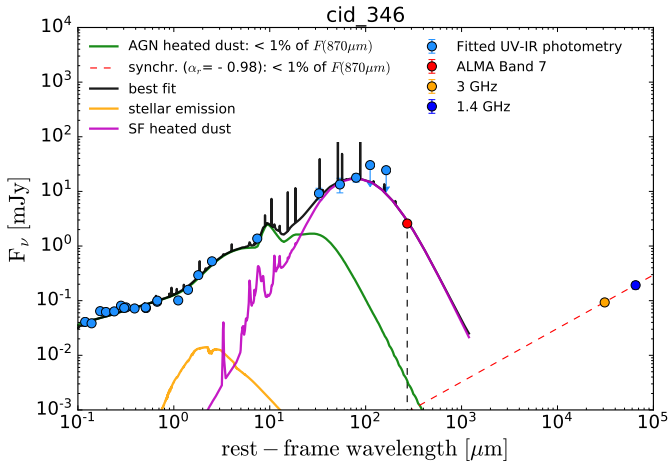


Fig. 5. Example rest-frame spectral energy distribution (SED) of one of our targets (cid_346). The light blue data points represent the UV-IR photometry used for the SED fit. The arrows indicate 3σ upper limits. The red point shows our ALMA Band 7 flux measurement (included in the fit). The blue and orange points show the radio fluxes at 1.4 and 3 GHz, respectively. The solid curves show the different components of the SED modelling performed with CIGALE. To estimate the maximum contribution of synchrotron emission to the rest-frame $260\ \mu\text{m}$ flux density, we parametrised this emission as a power law with spectral index $\alpha_r = -1.25$ (dashed red line), derived based on the 1.4 and 5.5 GHz data. The estimated contributions to the $260\ \mu\text{m}$ flux from dust heated by the AGN and from synchrotron emission are also shown.

Circosta et al. (2018) using AGN models from Fritz et al. (2006) and star-forming galaxies (SF) templates from Dale et al. (2014). We also show the curves corresponding to the average pure SF template and the average AGN only template from Stanley et al. (2018). They use AGN templates from Mullaney et al. (2011) and SF templates from Mullaney et al. (2011) and Silva et al. (1998).

All our targets are in the region between the SF and AGN templates, suggesting that the (observed-frame) $24\text{--}870\ \mu\text{m}$ emission is produced by a mixture of SF and AGN. The only two targets which are close to the AGN-dominated region of this diagram are cid_1057 and cid_451. These two targets are those with low S/N in the $870\ \mu\text{m}$ data ($S/N < 8$). This is probably reflecting the uncertainty in the measured $F_{870\ \mu\text{m}}$ fluxes and the higher fraction of flux that may be resolved out in the ALMA observations, rather than suggesting a higher AGN contribution.

To provide a more quantitative estimate of the contribution of the different physical processes to the rest-frame $260\ \mu\text{m}$ (observed-frame $870\ \mu\text{m}$) flux density of our targets, we also analyse the results of the UV-to-FIR SED fitting performed with CIGALE including our ALMA Band 7 photometric points (see Sect. 3.4). The MIR to FIR spectral range is modelled with two main components: emission by cold dust heated by SF and AGN emission due to the dusty torus peaking in the MIR. To estimate the AGN contribution to the $260\ \mu\text{m}$ flux density, we consider the ratio between the flux density of the AGN component at $260\ \mu\text{m}$ derived from the SED best-fit model and that measured from our ALMA data.

In Fig. 5, we show as an example the SED of one target (cid_346). The SEDs of the other targets are shown in Fig. E.1. The AGN contribution to the total flux at $260\ \mu\text{m}$ ranges from $<1\%$ to 6.3% (for cid_451), with a mean of 2.1% . Therefore, the results of the SED fitting decomposition suggest that the $260\ \mu\text{m}$ emission is dominated by star formation rather than heat-

ing from the AGN in all our targets. For the two targets with low S/N in the $870\ \mu\text{m}$ data (cid_1057 and cid_451), which are close to the AGN-dominated region of the diagnostic diagram from Stanley et al. (2018), the SED fitting would imply that the AGN only contributes 2.8% and 6.3% , respectively, to the $260\ \mu\text{m}$ flux. The CIGALE SED fitting code does not provide the uncertainties on the best-model SED. We therefore consider the uncertainties on the AGN fraction in the FIR range ($8\text{--}1000\ \mu\text{m}$), derived from the posterior distribution of the CIGALE SED fit. These uncertainties are in the range $3\text{--}10\%$. Thus, even adding these uncertainties, the AGN contribution remains small ($<16\%$). We note that the SED fit was performed including our ALMA high-resolution flux densities. We test that excluding the ALMA points from the SED fit, the inferred AGN contributions vary by less than 3% . Additionally, we test that using a difference SED fitting code (AGNfitter, Calistro Rivera et al. 2016), the AGN contributions remain small ($<7\%$).

We also consider a third method to estimate the AGN contribution in the FIR. The AGN re-processed emission depends on the model assumed to describe the torus, thus different models could potentially lead to different estimates. For the SED fitting, Circosta et al. (2018) use the models from Fritz et al. (2006). As an alternative approach, we model the torus emission using a modified black-body (MBB) following the methodology described by Lani et al. (2017). Using the AGN bolometric luminosity (L_{bol}) and the measured dust sizes (R_c), we apply Eq. (2) from Lani et al. (2017) to estimate the temperature that the dust heated by the AGN would have at a distance R_c from the AGN:

$$\left(\frac{T[\text{K}]}{1500}\right)^{\frac{4+\beta}{2}} = \frac{1}{R_c[\text{pc}]} \left(\frac{L_{\text{bol}}[\text{erg/s}]}{10^{46}}\right)^{\frac{1}{2}}. \quad (2)$$

We note that this equation assumes optically thin dust and we assume a dust emissivity index $\beta = 1.8$ for this test. For our sample, the temperatures of the AGN component (estimated using Eq. (2)) are in the range $68\text{--}153\ \text{K}$. Then, for each target we create a MBB with the estimated temperature and we scale this model to match the photometric data. In this way, we can estimate the maximum AGN contribution at rest-frame $260\ \mu\text{m}$ assuming a MBB model. Since this model is constrained only in the MIR range ($\sim 5\text{--}50\ \mu\text{m}$), we can apply it only to the six targets with enough photometric coverage in the MIR (i.e. excluding cid_1057 and cid_1143). The AGN contributions to the ALMA band 7 photometry estimated with this method are in the range $0.5\text{--}20\%$. These percentages are consistent within the uncertainties with the results from the CIGALE SED fitting. We consider more accurate the results from the CIGALE SED fitting, since this method uses a larger wavelength range to constrain the contribution from the AGN, including the near-infrared (NIR) photometry. Nevertheless, it is re-assuring that also using a different model to reproduce the torus emission returns consistent results.

Although we are limited by photometric coverage at long wavelengths in most of the SEDs, which makes the exact percentage of the AGN contribution uncertain, all our analyses indicate that the contribution from dust heated by the AGN to the $260\ \mu\text{m}$ emission, and hence to our maps produced from the ALMA data, is negligible. We note that some studies based on radiative transfer models have highlighted the possibility that AGN could contribute significantly to the heating of diffuse warm dust on host-galaxy scales (Schneider et al. 2015; Duras et al. 2017; Viaene et al. 2020; Di Mascia et al. 2021; McKinney et al. 2021). This emission is not related to the torus emission and therefore it is not taken into account in our SED

fitting decomposition. This AGN contribution is more important in the central region ($\lesssim 100$ pc, [Viaene et al. 2020](#)), but in more luminous AGN it could also affect larger scales. This effect on large scales is more likely to appear on extremely dusty and infrared-luminous objects, such as in infrared and submm selected galaxies ([McKinney et al. 2021](#)), or in very luminous quasars ($L_{\text{bol}} > 10^{47}$ erg s $^{-1}$, [Duras et al. 2017](#)), which is not the case of our sample. Detailed radiative transfer modelling would be required to test this effect on our sample, but this is beyond the scope of this work.

Synchrotron emission. In AGN, synchrotron emission can also contribute to the FIR flux, in particular in sources classified as ‘radio loud’ (e.g. [Dicken et al. 2008](#); [Falkendal et al. 2019](#)). All our targets have flux measurements or 3σ upper limits at 1.4 GHz and/or 3 GHz obtained with the Very Large Array (VLA). The radio fluxes are reported in [Circosta et al. \(2018\)](#). Briefly, the two sources from E-CDF-S (XID36 and XID419) have 1.4 GHz fluxes from [Miller et al. \(2013\)](#). XID36 has an additional flux measurement at 5.5 GHz taken with the Australia Telescope Compact Array (ATCA) from [Huynh et al. \(2012\)](#). X_N_81_44 has a 1.4 GHz flux upper limit from the VLA’s FIRST survey ([Becker et al. 1995](#)). The sources from COSMOS have flux measurements from the 3 GHz VLA-COSMOS project ([Smolčić et al. 2017](#)). Two targets (cid_346 and cid_451) have also a measurement at 1.4 GHz from [Schinnerer et al. \(2007\)](#).

To estimate the contribution from synchrotron emission to the ALMA Band 7 flux (rest-frame $\sim 260 \mu\text{m}$), we extrapolate from the radio fluxes using a power-law model ([Dicken et al. 2008](#)). For the two sources that have two flux measurements in the radio (XID36 and cid_346), we use the slope between the two points to determine the spectral index α_r ($F_\nu \propto \nu^{\alpha_r}$), assuming no significant variability in the radio at the two frequencies. For cid_346, we measure a spectral index $\alpha_r = -0.98$ and the contribution from synchrotron emission is 0.03%. For XID36 we measure a spectral index $\alpha_r = -1.25$ and a contribution of 0.06%. For cid_451, which is classified as a radio loud AGN, the 3 GHz flux is higher than the 1.4 GHz flux. Using the ALMA Band 3 flux at ~ 100 GHz from [Circosta et al. \(2021\)](#) and the 3 GHz flux, we estimate $\alpha_r = -0.99$ and a contribution of 21%. We note that since this source has low S/N, it is not included in our spatially resolved analyses. For the targets with only one flux measurement in the radio, we assume $\alpha_r = -0.7$, which is the median value measured for AGN from [Smolčić et al. \(2017\)](#). For these targets, the contribution from synchrotron emission is small ($< 1\%$). We note that even assuming a conservative value of $\alpha_r = 0$, which is towards the most extreme value measured for AGN ([Dicken et al. 2008](#); [Smolčić et al. 2017](#)), the synchrotron contribution is small ($< 34\%$ for cid_1057 (a source with low S/N in the ALMA map) and $< 14\%$ for the other targets).

We conclude that in our ALMA sample most of the emission at rest-frame $260 \mu\text{m}$ is due to dust heated by star formation, with contribution from dust heated by the AGN $\leq 6\%$ and synchrotron contribution $\leq 21\%$. If we consider only the six targets with high S/N in the $260 \mu\text{m}$ maps, the contribution from AGN-heated dust is $\leq 4\%$ and the synchrotron contribution is $< 1\%$. The estimated contributions for each target are tabulated in Table 2.

5.2. FIR size comparison with other samples from the literature

In this section, we compare the FIR sizes of our sample with other samples of galaxies at similar redshift from the literature. We also investigate if there is any difference in the size of galaxies with and without an AGN.

From our analysis, we find that the FIR effective radii derived from the fit with the ‘preferred models’ for our sample are in the range 0.80–2.01 kpc, with a mean of 1.36 ± 0.21 kpc. These sizes are comparable to previous measurements presented from ALMA data for $z \sim 1\text{--}3$ AGN and star-forming galaxies ([Barro et al. 2016](#); [Hodge et al. 2016](#); [Fujimoto et al. 2017](#); [Gullberg et al. 2019](#); [Scholtz et al. 2020](#); [Chen et al. 2020](#)).

We investigate in more detail how our sizes compare to other samples in Fig. 6, where we plot size as a function of observed-frame $870 \mu\text{m}$ flux density. We show the 6/8 sources with high S/N in our sample. For the sake of a more direct comparison to literature, we show the sizes from our exponential and Gaussian fits (see Sect. 3.3.1; Appendix B), noting that these are consistent with the sizes derived from our ‘preferred’ models.

For this comparison, we identify five samples of star-forming galaxies (SFGs) and AGN with (i) similar redshifts to our sample ($z \sim 1.5\text{--}2.5$) and (ii) FIR sizes measured from high-resolution ($< 0.5''$) ALMA Band 7 continuum data: [Hodge et al. \(2016\)](#), [Gullberg et al. \(2019\)](#), [Scholtz et al. \(2020\)](#), [Chen et al. \(2020\)](#), and [Tadaki et al. \(2020\)](#). We consider only the sources detected with $S/N > 8$, for which it is possible to derive reliable sizes. In Table 4 we summarise the main properties of the literature samples (sample size, redshift, resolution and rms sensitivity of the ALMA maps, and the model used to derive the FIR sizes).

The first sample consists of 16 sub-millimetre galaxies (SMGs) from the ALESS survey ([Hodge et al. 2013](#); [Karim et al. 2013](#)), whose FIR sizes are reported in [Hodge et al. \(2016\)](#). We consider only the SMGs in the redshift range $z = 1.5\text{--}2.5$ (six objects). Based on X-ray data ([Wang et al. 2013](#)), one object (ALESS17.1) is confirmed as AGN. We note that two of the targets have X-ray luminosities $L_X(0.5\text{--}8 \text{ keV}) > 10^{42.2}$ erg s $^{-1}$, for which it is ambiguous if the emission is due to an AGN or to star formation.

The second sample is presented by [Gullberg et al. \(2019\)](#). They measure the FIR sizes from exponential fits for 153 SMGs from the ALMA SCUBA-2 UDS survey (AS2UDS; [Stach et al. 2019](#)). Using MIR diagnostics, [Stach et al. \(2019\)](#) identified one third of the sample as AGN, one third as non-AGN, with the final third having insufficient MIR photometry for this classification. Using stacking analyses, [Gullberg et al. \(2019\)](#) show that their measured individual sizes underestimate the true sizes by $\sim 50\%$ due to the relatively low rms (median of $0.3 \text{ mJy beam}^{-1}$ compared to our mean $0.02 \text{ mJy beam}^{-1}$). Therefore, in Fig. 6, we just show their derived median size which accounts for this effect.

The third sample is presented in [Scholtz et al. \(2020\)](#) and consists of eight X-ray AGN at $z = 1.4\text{--}2.6$ from the KMOS AGN Survey at High-redshift (KASHz)¹³. We exclude from the comparison two targets with low-resolution ALMA data (beam size $> 0.5''$) and two targets with $S/N < 8$.

Moreover, we consider the sample of six SMGs in the redshift range $z = 1.5\text{--}2.5$ presented by [Chen et al. \(2020\)](#). Three objects are classified as X-ray AGN, one as infrared AGN, and two as non-AGN. Two targets are also present in the sample from [Hodge et al. \(2016\)](#) and have consistent size measurements, thus we consider them only once in our comparison.

Finally, we consider the sample of 62 massive ($M_\star > 10^{11} M_\odot$) star-forming galaxies at redshift $z = 1.9\text{--}2.6$ from [Tadaki et al. \(2020\)](#). X-ray data for this sample are available from [Luo et al. \(2017\)](#) and [Kocevski et al. \(2018\)](#). Based on a

¹³ We note that [Scholtz et al. \(2020\)](#) reported the effective radii as $R_e = \sigma = FWHM/2.355$. For our comparison, we convert their size measurements to $R_e = FWHM/2$, to be consistent with our definition.

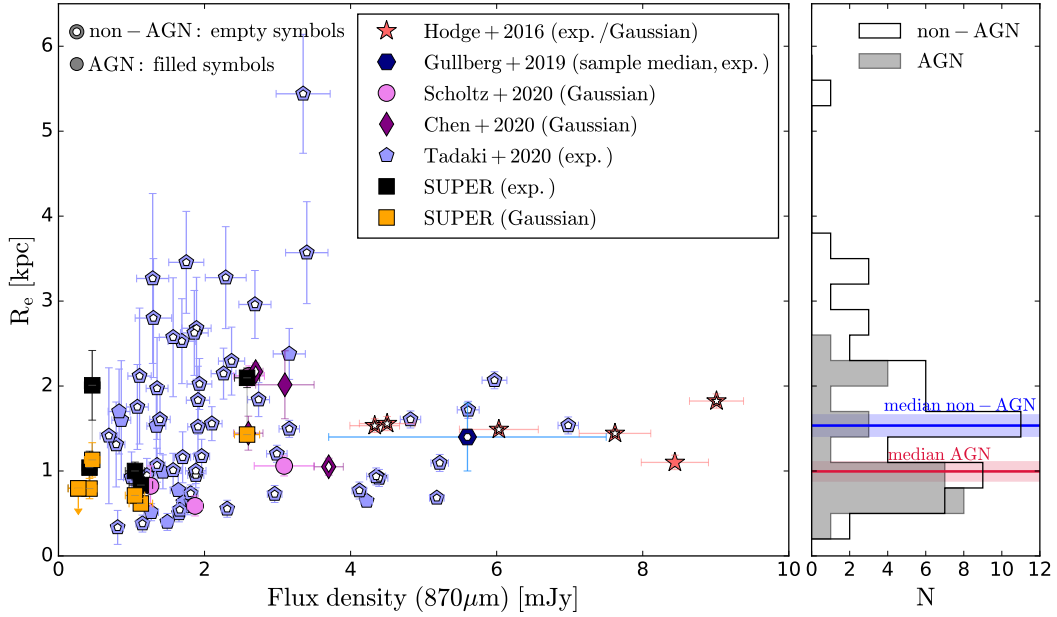


Fig. 6. FIR effective radii versus observed-frame $870\mu\text{m}$ flux density for our targets and other samples from the literature at similar redshift ($z \sim 2$), derived from ALMA observations at similar resolution ($\sim 0.2''$). The effective radii are measured assuming a Gaussian profile for the Scholtz et al. (2020) and Chen et al. (2020) samples; an exponential profile for the Gullberg et al. (2019) and Tadaki et al. (2020) sample; and a Sérsic profile with index n between Gaussian and exponential for the Hodge et al. (2016) sample. For the Gullberg et al. (2019) sample, we show the median value of the sample. For SUPER, we show the radii measured from the fit of the visibilities assuming both a Gaussian and an exponential profile. Filled symbols are used for AGN and empty symbols for galaxies with no AGN signature. The Gullberg et al. (2019) sample is a mixture of AGN and non-AGN. The histograms on the right show the distributions of FIR effective radii for AGN (filled histogram) and star-forming galaxies with no AGN (empty histogram), with the corresponding medians.

Table 4. Properties of the literature samples used to compare the FIR sizes (see Sect. 5.2).

Reference	N	z	rms [mJy beam $^{-1}$]	Resolution [arcsec]	Model	$\langle R_e \rangle$ [kpc]
	(1)	(2)	(3)	(4)	(5)	
This work	6	2.1–2.5	0.02–0.04	0.16–0.27	Exp. (Gaussian)	1.31 ± 0.23 (0.93 ± 0.23) ^(a)
Hodge et al. (2016)	6	1.5–2.5	~ 0.064	~ 0.16	Exp./Gaussian ^(b)	1.48 ± 0.08
Gullberg et al. (2019)	153	1.5–5.8 (median 2.9)	0.09–0.34	~ 0.18	Exponential	1.20 ± 0.4
Scholtz et al. (2020)	4	1.4–2.6	0.02–0.69	0.16–0.28	Gaussian	0.97 ± 0.24
Chen et al. (2020)	4	1.5–2.5	0.03–0.07	0.17–0.25	Gaussian	1.67 ± 0.22
Tadaki et al. (2020)	62	1.9–2.6	~ 0.06	0.20–0.30	Exponential	1.56 ± 0.12

Notes. (1) Number of objects considered in our comparison. (2) Redshift of the sources. (3) rms sensitivity of the ALMA observed-frame $870\mu\text{m}$ maps. (4) Resolution of the ALMA observed-frame $870\mu\text{m}$ maps. (5) Model used to measure the FIR sizes: exponential (exp.) or Gaussian. (6) Mean FIR size (half-light radius) derived from the $870\mu\text{m}$ data. ^(a)For our work, we report the mean R_e obtained using both the exponential (exp.) and the Gaussian model. ^(b)Hodge et al. (2016) fit the sample assuming a Sérsic profile with index n free. The six SMGs with $z = 1.5$ – 2.5 have FIR profiles between Gaussian and exponential (Sérsic index $n = 0.5$ – 1).

threshold of intrinsic X-ray luminosity $L_X > 10^{42} \text{ erg s}^{-1}$, 13 objects are classified as AGN. We note that this sample combines high-resolution ALMA observations ($0.2''$) with a compact array configuration (maximum recoverable scale $\sim 6.7''$). Therefore, their observations are more sensitive to large scales than the other samples, which only use the high-resolution configuration.

The mean effective radius obtained with the exponential fit for our sample ($1.30 \pm 0.22 \text{ kpc}$) is consistent with the mean sizes from Hodge et al. (2016) ($1.48 \pm 0.08 \text{ kpc}$), Gullberg et al. (2019) ($1.20 \pm 0.4 \text{ kpc}$), and Tadaki et al. (2020) ($1.56 \pm 0.12 \text{ kpc}$), that also used the exponential fit. Using the Gaussian fit, we obtained a mean radius of $0.91 \pm 0.11 \text{ kpc}$, which is consistent with Scholtz et al. (2020) ($1.14 \pm 0.29 \text{ kpc}$) and smaller (by $>3\sigma$) than the mean size from Chen et al. (2020) ($1.67 \pm$

0.22 kpc), both obtained assuming a Gaussian profile. However, we note that our sample has a smaller range of flux densities ($F_{870\mu\text{m}} = 0.3$ – 2.6 mJy) compared to these other samples ($F_{870\mu\text{m}} = 0.7$ – 9.0 mJy), which include also SMGs, that is galaxies selected because of their high submm flux. If we limit the comparison to objects with $F_{870\mu\text{m}} < 2.6 \text{ mJy}$, the mean size derived, $1.44 \pm 0.11 \text{ kpc}$, is consistent with the mean size of our sample (measured with the exponential fit).

We also separate the sample in AGN and non-AGN (see open and filled symbols in Fig. 6), to investigate whether there is a difference in their FIR sizes. We consider the sizes measured assuming a Gaussian profile, when possible, in order to have a consistent method for all samples. We note that for the Tadaki et al. (2020) sample this is not possible, since the sizes

have been measured only with the exponential profile. However, we note that if we were to use the sizes measured with the exponential profile fit, we would obtain the same qualitative results. We exclude from this analysis the sample from Gullberg et al. (2019), for which we only have the ‘median’ size of the sample that includes both AGN and non-AGN.

The mean size for AGN is 1.16 ± 0.11 kpc, while the mean size for non-AGN is 1.69 ± 0.13 kpc (4σ difference). Applying the two-samples Kolmogorov–Smirnov (KS) test, we find a p -value = 0.03, meaning that the distributions of sizes for the AGN and non-AGN are significantly different (p -value < 0.05). We note that if we consider the sizes measured only with exponential or only with Gaussian profiles, the KS test finds a significant difference between the sizes of AGN and non-AGN with p -values of 0.02 and 0.01, respectively. The AGN sample has a low mean flux density ($F_{870\mu\text{m}} = 2.0 \pm 0.3$ mJy) compared with the non-AGN sample ($F_{870\mu\text{m}} = 2.8 \pm 0.2$ mJy). Therefore, it is possible that the difference in FIR sizes is partly related to the difference in flux density, and not to the presence of an AGN. To test this, we limit the samples to objects with flux densities < 4 mJy, and we find that the difference between AGN and non-AGN becomes even larger: the mean size for AGN is 1.18 ± 0.12 kpc and for non-AGN is 1.80 ± 0.16 kpc (p -value of the KS test is 0.03). The AGN sample has a stellar mass distribution slightly skewed to lower stellar masses (30% of objects have $M_\star < 10^{10} M_\odot$, median $M_\star = 10^{11.07} M_\odot$), compared with the non-AGN sample (3% of objects have $M_\star < 10^{10} M_\odot$, median $M_\star = 10^{11.21} M_\odot$). If we consider only objects with $M_\star > 10^{11} M_\odot$, we still find a significant difference in the mean size of AGN (1.06 ± 0.14 kpc) and non-AGN (1.70 ± 0.10 kpc).

As mentioned before, the observations of Tadaki et al. (2020) are more sensitive to large scales than the other samples, and therefore they may be more effective in recovering larger and more diffuse dust emission. This could introduce a bias in our comparison. To avoid it, we compare the sizes of AGN and non-AGN within the Tadaki et al. (2020) sample. We note that there is no significant difference in the stellar mass or SFR distribution of the AGN and non-AGN within this sample. Using the KS test, we find that the FIR sizes of AGN are significantly smaller than the ones of non-AGN (p -value = 0.03). To take into account the uncertainties in the size measurements, we apply a Monte Carlo approach. For each source, we draw 100 samples from a Gaussian distribution centred on the measured size and with standard deviation equal to the uncertainty on the size. Then we perform the KS test on the drawn samples. In 79% of the samples, the KS test gives a p -value < 0.05, meaning that the difference is significant at the 79% level.

Some previous studies have also found smaller FIR sizes in galaxies hosting AGN. For example, Chang et al. (2020) also find smaller sizes in obscured IR-selected AGN compared to non-AGN at $z \sim 1$. Stacey et al. (2021) find that the host galaxies of lensed quasars at $z = 1.5 - 2.8$ generally have smaller sizes than dusty star-forming galaxies of similar infrared luminosity. Furthermore, Lutz et al. (2018) find smaller FIR sizes in nearby ($z < 0.06$) X-ray selected AGN than in non-AGN at the same FIR luminosity. Under the assumption that the dust is spatially coincident with the gas reservoir, their interpretation is that a compact configuration of dust and gas favours the accretion to the central SMBH. However, another interpretation is that the AGN are contributing significantly to the heating of the diffuse dust in the central region of the galaxy, resulting in more concentrated FIR emission in AGN host galaxies (e.g. Schneider et al. 2015; Viaene et al. 2020; Di Mascia et al. 2021; McKinney et al. 2021). On the other hand, Ni et al. (2021) recently reported a

relation between the black hole accretion rate and the compactness of the host galaxy using optical/NIR imaging. They also interpret this relation as a link between the black hole growth and the central gas density.

The significance of the difference in dust size between AGN and non-AGN presented in this paper is still limited by the sample size and by the lack of homogeneity in the samples (although we have tried to minimise these as much as possible). In order to confirm our result, it would be important to have a larger AGN and control samples well matched in SFR, stellar mass, redshift and with similar FIR sensitivity and resolution.

5.3. Ionised gas and FIR emission

5.3.1. Origin of the H α emission

The H α emission is sometimes used to trace the spatial distribution of unobscured star formation in AGN host galaxies. Previous studies have performed a variety of analyses to try to minimise the challenges in using H α maps to investigate the impact of AGN outflows on star formation (Cano-Díaz et al. 2012; Cresci et al. 2015a; Carniani et al. 2016). These challenges include the fact that part of the H α flux could be due to the ionising radiation of the AGN itself, and therefore special care should be taken if we want to use it as a star formation rate tracer (e.g. Scholtz et al. 2020). In addition, H α can suffer from significant obscuration (see also Kewley et al. 2013a; D’Agostino et al. 2019). Therefore, if we want to use H α as a SFR tracer we need to determine what is the dominant contributor to the line emission and whether we can identify a component of the H α emission that can be used to trace star formation in our sample.

Unlike Carniani et al. (2016), we were unable to identify any residual emission beyond the components associated with the AGN (i.e. the broad-line regions, AGN narrow line regions and outflows, see Sect. 4.4). Therefore, we may expect the H α emission we have mapped to be dominated by AGN-related processes. To verify this, in Fig. 7 we use a BPT-like diagram (Baldwin et al. 1981) which uses the optical line ratios [O III]/H β and [N II]/H α to separate galaxies depending on the different source of ionisation (HII region or AGN).

The black dashed curve is the separation between star formation and ‘composite’ (AGN/star-forming) at the mean redshift of our sample ($z = 2.3$) from Kewley et al. (2013b). As a reference, we also show as a grey dashed curve the separation at $z = 0$ (Kauffmann et al. 2003). The upper panel shows the line ratios measured from the total line profiles (narrow and broad component), while the lower panel shows the line ratios of only the narrow components. In the cases where H β is not detected, based on a detection threshold of $S/N > 3$, we derive a 5σ lower limit for the [O III]/H β line ratio (see Sect. 4.3). Similarly, for the cases where [N II] is not detected, we show the 5σ upper limit for the [N II]/H α line ratio. In some targets, both the H α and [N II] lines are not detected, therefore the [N II]/H α line ratio is unconstrained (see box on the right).

Most of our objects lie above the division line when we consider the line ratios measured from the total profile (see upper panel of Fig. 7). This means that the emission is not dominated by star formation. This is not surprising, since these are X-ray selected AGN. For two objects, the [N II]/H α line ratio is unconstrained. If we assume that they have a similar [N II]/H α line ratio as the other objects, they would be in the AGN region. The only target which lies in the HII region is cid_346.

The targets remain in the same region of the BPT diagram also when considering only the narrow component (see lower panel of Fig. 7). This again is not surprising given the fact that

our targets are bright AGN. Therefore, even if we were to consider the narrow component separately, it would still be dominated by AGN emission in most of our galaxies. The only exception is cid_346, which lies in the HII part of the diagram both when considering the total profile and when considering only the narrow component. For this target, we do not see a large difference in the spatial distribution of the ‘narrow’ map and the map that contains both the narrow and broad components. Thus, our main conclusions would not change if we were to consider only the narrow H α component for cid_346.

In summary, the BPT analysis suggests that H α emission is dominated by AGN ionisation in most of our sample. As discussed in the next section, the central position of H α and [O III] are in agreement for most targets (see Fig. 8). Our sources lie within the scatter of the [O III]-X-ray luminosity relation derived by Kakkad et al. (2020) using data from SUPER and from X-ray selected AGN at $z \sim 1.1$ –2.5 from the KASHz survey (Harrison et al. 2016b). This suggests that the [O III] emission is mainly ionised by the AGN, as traced by the X-rays. Consequently, the similar spatial distribution of H α and [O III] supports the idea that also the H α emission is predominantly ionised by the AGN.

For this analysis, we have considered spatially integrated spectra, but there may be spatial variations in the line ratios and some of the emission is probably more AGN dominated (e.g. towards the centre). Unfortunately, with the current resolution we are not able to investigate spatial variations or de-couple AGN and star formation contributions as done in Cano-Díaz et al. (2012), Cresci et al. (2015a) and Carniani et al. (2016). Additionally, PSF-smearing could spread the AGN emission from the central spaxels to the other spaxels, contaminating the H α emission at larger scales, which may be originally dominated by star formation.

Summarising, we are not able to use the H α emission as a good indicator of short term (~ 10 Myr) star formation in our sample. The FIR emission can provide information on the spatial location of the dust-obscured star formation, but in general it can trace SFR up to longer timescales (up to 100 Myr, Kennicutt & Evans 2012). As an alternative to H α , star formation on short timescales can be traced using rest-frame UV observations, which however could suffer from AGN contamination and dust-obscuration as well.

5.3.2. Comparison of spatial distribution of FIR, optical, H α , and [O III] emission

In this section we compare the spatial distribution of the FIR, optical, H α and [O III] emission. In Fig. 3, we show the FIR continuum contours, with the [O III] and H α contours overlaid, created using the ‘central’ 600 km s $^{-1}$ wide maps. We measure the positions of the FIR, H α and [O III] emission by fitting a 2D Gaussian to the images using the python routine `scipy.optimize.curve_fit` (see Sect. 4.4). The positions of the centroids are plotted as crosses on the images, with circles indicating the corresponding 1σ uncertainties. The position of the rest-frame optical continuum (see Sect. 4.2) is also shown in lightblue.

In Fig. 8 we directly compare the difference in position between the FIR continuum, optical continuum, H α and [O III] emission. The two targets with low S/N in the ALMA maps are marked with empty symbols.

The rest-frame optical continuum emission is in general agreement with the position of the FIR continuum (see left panel

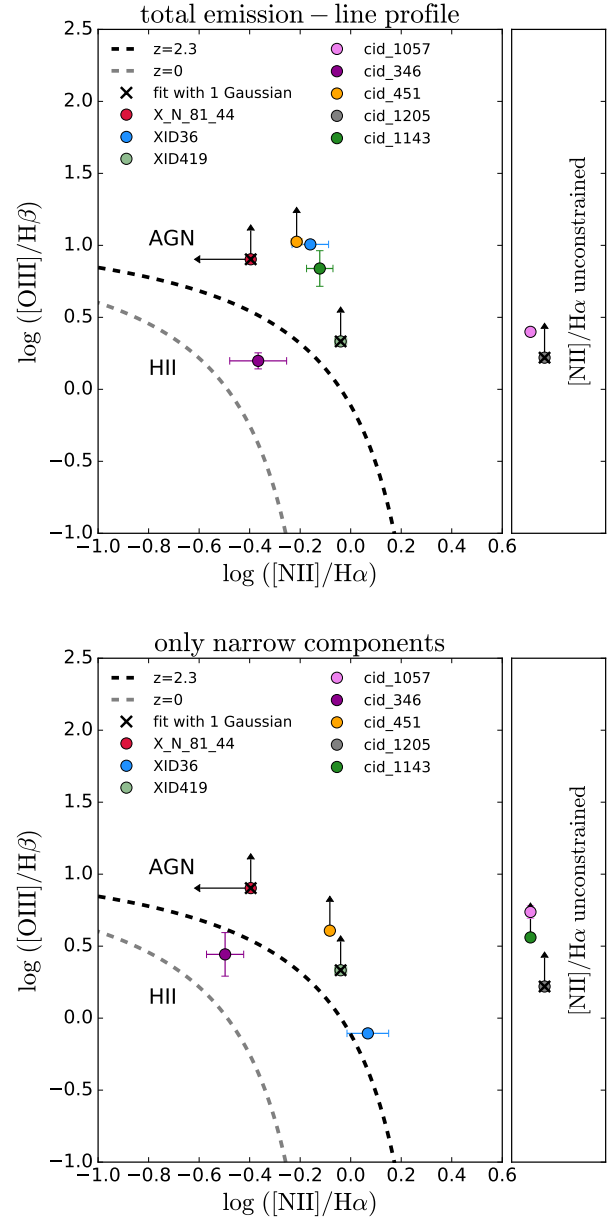


Fig. 7. Emission lines diagnostic diagrams. The curves show the separation between star-forming galaxies and AGN at redshift $z = 0$ (grey) and $z = 2.3$ (black) from Kewley et al. (2013a). In the cases where one line is not detected ($S/N < 3$), the line ratio is shown with an arrow indicating a 5σ upper (or lower) limit. In the cases where both the H α and [N II] lines are not detected, the [N II]/H α line ratio is unconstrained (see box on the right). *Upper panel:* the line ratios are measured from the total emission line profile. *Lower panel:* the line ratios are calculated using the fluxes of only the narrow Gaussian component. For the three targets for which the emission lines were fitted with only one Gaussian component (marked with black crosses), the line ratios are the same as in the upper panel.

of Fig. 8). The offset between optical and FIR continuum is smaller than the uncertainties for all targets, with the exception of cid_1057 and X_N_81_44. cid_1057 has low S/N in the ALMA maps ($S/N = 3.6$), therefore, the FIR position is not well constrained. X_N_81_44 shows an offset larger than the uncertainties, but still small ($< 0.05''$). In the Type 1s, the optical continuum is dominated by the AGN emission, while in the Type 2s it is probably tracing the stellar disk, since the central

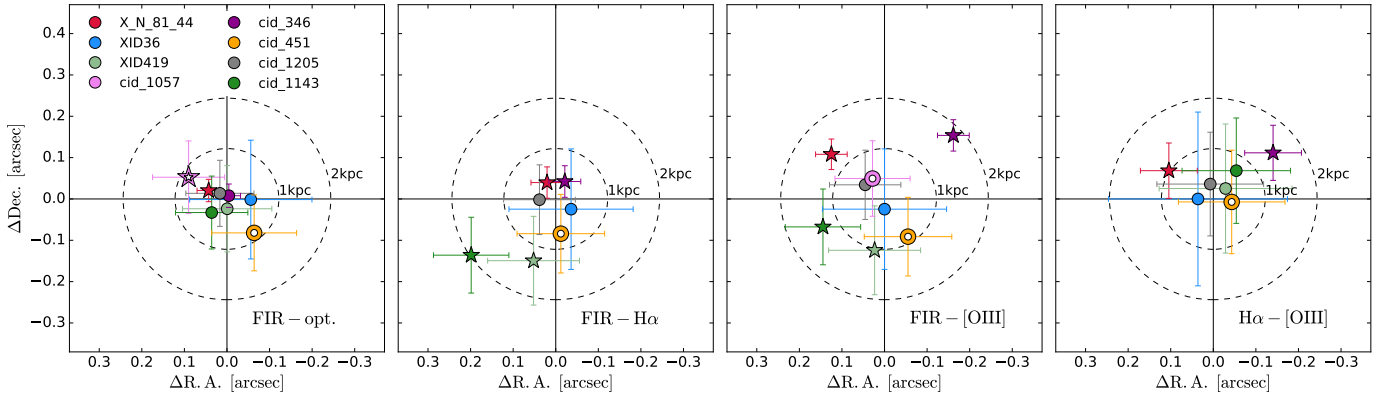


Fig. 8. Comparison of the centroid positions of the 2D Gaussian fit to the images of (*from left to right*): FIR and optical continuum, FIR and $H\alpha$ emission, FIR and [O III] emission, and $H\alpha$ and [O III] emission. The coordinates are derived from the centroid of a 2D Gaussian fit to the images. The $H\alpha$ and [O III] images were created by integrating the spectra over the $[-300, 300]$ km s^{-1} velocity range. The uncertainties on the position combine the uncertainties on the coordinate registration, on the Gaussian fit and the pixel size. The objects with a significant offset (i.e. difference in RA or Dec larger than the 1σ uncertainty) are shown as star symbols in each plot, while the ones with no significant offset are shown as circles. The dashed circles show the offset corresponding to 1 kpc and 2 kpc at the median redshift of the sample. The two objects with ALMA low $S/N < 8$ are shown as empty symbols (cid_1057 and cid_451). The position of the $H\alpha$ and [O III] centroids are in fairly good agreement, while the FIR centroids show larger offset to the centroid positions of the ionised gas (both $H\alpha$ and [O III]).

AGN is obscured. The good alignment between the FIR continuum emission and the optical continuum suggests that the FIR is aligned with the host galaxy position. Unfortunately, we do not have other information about the host galaxy morphology. For three sources, there are HST/WFC3 images available, but the images show only strong point sources, so we cannot derive any information about the host galaxy morphology.

For the majority of the sources with reliable FIR positions (4/6), the $H\alpha$ and [O III] centroid positions are not consistent with the FIR position (difference larger than 1σ , see Fig. 8). The offsets between the FIR and $H\alpha$ position are in the range 0.3–1.9 kpc, with a mean offset of 0.8 ± 0.2 kpc. The offsets between the FIR and [O III] are in the range 0.2–1.8 kpc, with a mean offset of 1.0 ± 0.2 kpc. Two objects have an offset > 1 kpc, both for $H\alpha$ and [O III]: XID419 and cid_1143. We compare our results with the work by Scholtz et al. (2020), who measured the offset between the FIR emission and the $H\alpha$ emission in a sample of eight AGN at redshift 1.4–2.6. They found projected offsets between $H\alpha$ and FIR in the range 0.8–2.8 kpc, with a mean offset of 1.4 ± 0.6 kpc. The offsets found by Scholtz et al. (2020) are a bit larger but consistent with our findings. However, we note that their rest-frame optical observations have a lower spatial resolution (FWHM PSF ~ 0.6 – $1''$) compared to the AO observations presented here.

To summarise, we find that the centroid of the FIR emission is on average offset ($> 1\sigma$, see star symbols in Fig. 8) from the [O III] and $H\alpha$ centroids. However, we note that there can still be significant overlap between the emissions even if the centroids are offset. One possible explanation of the offset is that the dust and the ionised gas have different locations. Another possibility is that the outflow component is contributing substantially also in the central velocity channel ($v = [-300, 300]$ km s^{-1}). In the next Sect. 5.4, we compare the position of the [O III] emission in the central velocity channel with the emission in the blue-shifted and red-shifted channels ($v < -300$ km s^{-1} and $v > 300$ km s^{-1}). For XID36 and cid_451, the morphology and position of the [O III] emission is similar in the three velocity channels, which suggests that the outflow component may contribute significantly also in the central velocity channels. For the other targets, the morphology and position of the emission in the three channels are dif-

ferent, suggesting that the central [O III] channel is not strongly contaminated by the outflow component.

It is also possible that the dust is obscuring part of the $H\alpha$ and [O III] emission, especially where the peak of the dust emission is located. Unfortunately, in most of our objects, we do not have a measurement of the Balmer decrement, because of the low S/N of the $H\alpha$ and $H\beta$ emission lines. However, even the Balmer decrement could underestimate the level of obscuration, because in the most obscured regions the ionised gas emission may be totally obscured by dust (see Chen et al. 2020). The fact that the $H\alpha$ and FIR emission are not co-spatial has implications if we want to use the $H\alpha$ emission to trace the total star formation in the host galaxies. First, the assumption that $H\alpha$ emission is dominated by star formation is likely not to be true in most of our cases (see Sect. 5.3.1). Second, even if we could derive the extinction correction for the $H\alpha$ emission, we would still not be able to recover the total SFR of the galaxy since we would not be sampling the same region as that covered by the FIR emission (e.g. Brusa et al. 2018).

In Fig. 3, which presents the $H\alpha$ and [O III] maps, we also show the position angle along the major axis of the FIR emission for the three targets where it can be reliably determined (XID419, cid_346, and cid_1143). The $H\alpha$ and [O III] emission are offset from the FIR emission in a direction roughly perpendicular to the FIR major axis. This could be indicative of AGN ionisation cones, extending perpendicular to the plane of the galaxy (e.g. Crenshaw et al. 2010; Venturi et al. 2017, 2018). This would favour a scenario where a significant fraction of the ionised gas has a different locations with respect to the FIR emission. However, we cannot rule out that dust is obscuring part of the ionised gas emission.

The $H\alpha$ and [O III] positions are in general in agreement with each other, with offsets in the range 0.3–1.5 kpc and mean offset 0.6 ± 0.1 kpc (see fourth panel in Fig. 8). Only two objects (X_N_81_44 and cid_346) show a $H\alpha$ –[O III] offset larger than the uncertainties. In X_N_81_44 the morphologies of $H\alpha$ and [O III] emission are also different, extending in two almost perpendicular directions. In cid_346 instead the $H\alpha$ distribution is similar to the FIR distribution, while [O III] is more extended in the S-E direction. We note that cid_346 is the only object in

our sample which is classified in the HII region according to the emission line diagnostic diagram (see Sect. 5.3.1). The offset between H α and [O III] could be a result of the fact that they are ionised by different mechanisms (AGN for [O III] and star formation for H α).

Following Chen et al. (2020) and Scholtz et al. (2020), we also compare the sizes of the FIR, H α , and [O III] emission in Fig. 9. We use the FIR sizes derived with the best model fit of the uv -visibilities. In general, the H α and [O III] sizes are comparable or larger than the FIR sizes. The only exception is cid_1143, for which the upper limits on the H α and [O III] sizes are smaller than the FIR sizes. We note that the FIR emission of this object is significantly elongated (axis ratio = 4.6). A possible interpretation is that the dust emission is tracing the stellar disk of this galaxy (seen edge-on), and the ionised gas is more extended out of the galaxy plane. The mean ratios are $R_e(\text{H}\alpha)/R_e(\text{FIR}) = 1.87 \pm 0.45$ and $R_e([\text{O III}])/R_e(\text{FIR}) = 1.50 \pm 0.23$. Larger H α sizes compared to FIR sizes have also been observed by Scholtz et al. (2020), Chen et al. (2020) and Tadaki et al. (2020), who find mean ratio $R_e(\text{H}\alpha)/R_e(\text{FIR})$ of 3.1 ± 0.6 , 2.1 ± 0.3 , and 2.3 respectively. These studies find on average larger H α sizes (and larger $R_e(\text{H}\alpha)/R_e(\text{FIR})$ ratios) compared to our observations. The difference could be due to the fact that our AO observations are missing part of the more extended flux (Förster Schreiber et al. 2018). Additionally, in our case we cannot exclude that the FIR sizes are underestimated because the high-resolution ALMA observations are not sensitive to more diffuse emission.

The larger sizes of the ionised gas emission compared to the FIR sizes could be due to different reasons. One possibility is that the ionised gas is more extended because of the AGN, that ionises the gas to larger distances (e.g. Scholtz et al. 2020). However, larger H α sizes compared to the FIR have been observed also in star-forming galaxies not hosting AGN (Chen et al. 2020; Tadaki et al. 2020). In $z \sim 2$ star-forming galaxies, the optical continuum is found to be systematically larger than the FIR sizes by a factor of 2–3, suggesting that the FIR emission is tracing a compact star-burst region (e.g. Barro et al. 2016; Tadaki et al. 2017; Fujimoto et al. 2017, 2018; Elbaz et al. 2018; Calistro Rivera et al. 2018; Lang et al. 2019; Puglisi et al. 2019). It is interesting to note that Popping et al. (2021) use simulations to show that the larger rest-frame optical sizes are due to higher dust-obscuration in the centre of galaxies which artificially increases the derived sizes in this band, and that the FIR emission is not intrinsically more compact than the stellar distribution.

5.4. Ionised outflows and star formation

In this section, we qualitatively compare the spatial distribution of the [O III] outflows and star formation. As we have shown in Sect. 5.1, the rest-frame 260 μm emission in our targets is mostly due to star formation, while we cannot rely on the H α emission as a star formation indicator. Thus, here we focus on the spatial comparison of the outflows and FIR emission.

Following Kakkad et al. (2020), we define as outflow the [O III] emission with absolute velocities $>300 \text{ km s}^{-1}$ with respect to the zero velocity (see Sect. 4.4). In Fig. 10 we show the [O III] maps in three velocity channels: blue-shifted emission $<-300 \text{ km s}^{-1}$, central emission $[-300, 300] \text{ km s}^{-1}$, and red-shifted emission $>300 \text{ km s}^{-1}$. We create the maps by collapsing the continuum subtracted spectra over the selected velocity channels for each spaxel. We check that our conclusions are not sensitive to the choice of the threshold adopted to select the blue- or red-shifted emission (i.e. absolute velocities $>300 \text{ km s}^{-1}$). By

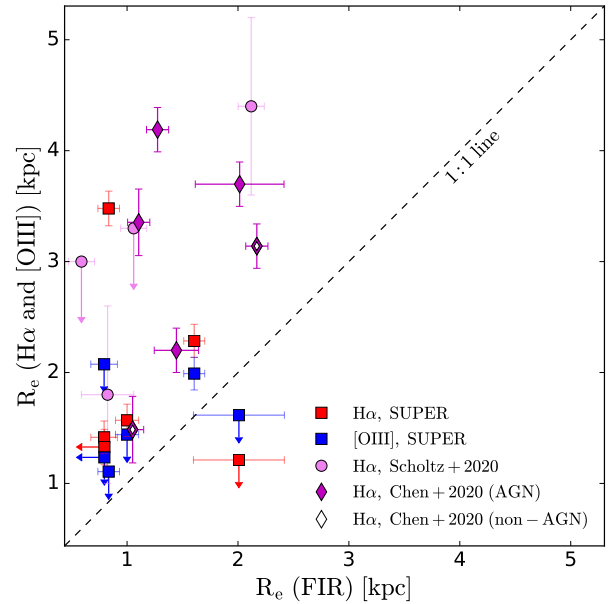


Fig. 9. Comparison of the size of the FIR emission with the sizes of the H α (red) and [O III] (blue) emission. The effective radii of the FIR emission are measured from the best fit on the visibilities. The H α and [O III] sizes are measured by fitting a 2D Gaussian to the images. If the measured size is smaller than the beam, we show the point as an upper limit. The two objects with low S/N (<8) in the ALMA data are not shown (cid_1057 and cid_451). The FIR and H α sizes of the sample of $z \sim 2$ AGN from Scholtz et al. (2020) and from Chen et al. (2020) are shown with violet circles and magenta diamonds, respectively. The white diamonds are non-AGN from Chen et al. (2020). On average, the FIR sizes are smaller than the H α and [O III] sizes by a factor of ~ 2 .

selecting only the extreme velocity wings (e.g. $>600 \text{ km s}^{-1}$), the qualitative conclusions remain the same.

All our targets apart from cid_1205 show blue-shifted emission (above 4σ), in agreement with the analyses of Kakkad et al. (2020) on the Type 1 targets. We note that the [O III] data-cube of cid_1205 presents an artefact (horizontal stripe) south of the target. After removing the artefact, we do not see significant emission in the blue-shifted map, but we cannot exclude that a faint outflow could be undetected. However, since the [O III] spectrum of this target shows only a weak emission at velocities $<-300 \text{ km s}^{-1}$, we do not expect a strong [O III] outflow in this target.

From the [O III] line profiles, we can see that the blue-wing is generally more prominent than the red-wing. This effect can be due to dust that is obscuring the receding side of the outflow (e.g. Bae & Woo 2016). The more extended blue-shifted emissions ($>4.5 \text{ kpc}$) are detected in cid_1143, and cid_1057. The red-shifted emission is fainter and detected above 5σ in only 5/8 objects (X_N_81_44, XID36, cid_1057, cid_451 and cid_1205). These objects show a significantly extended ($\sim 2.5 \text{ kpc}$) red-shifted emission.

The shape of the outflow is certainly also a function of the viewing angle. In XID36 and cid_451, the blue-shifted emission is symmetric (not elongated) and the shape is similar to the emission in the central velocity channel. A possible interpretation is that the outflow is aligned in the direction of our line-of-sight. On the contrary, in cid_1143 and cid_1057 the outflow has an extended and biconical shape which is suggesting that our line of sight is almost perpendicular to it. In particular, in cid_1143, the direction of the outflow is perpendicular to the major axis

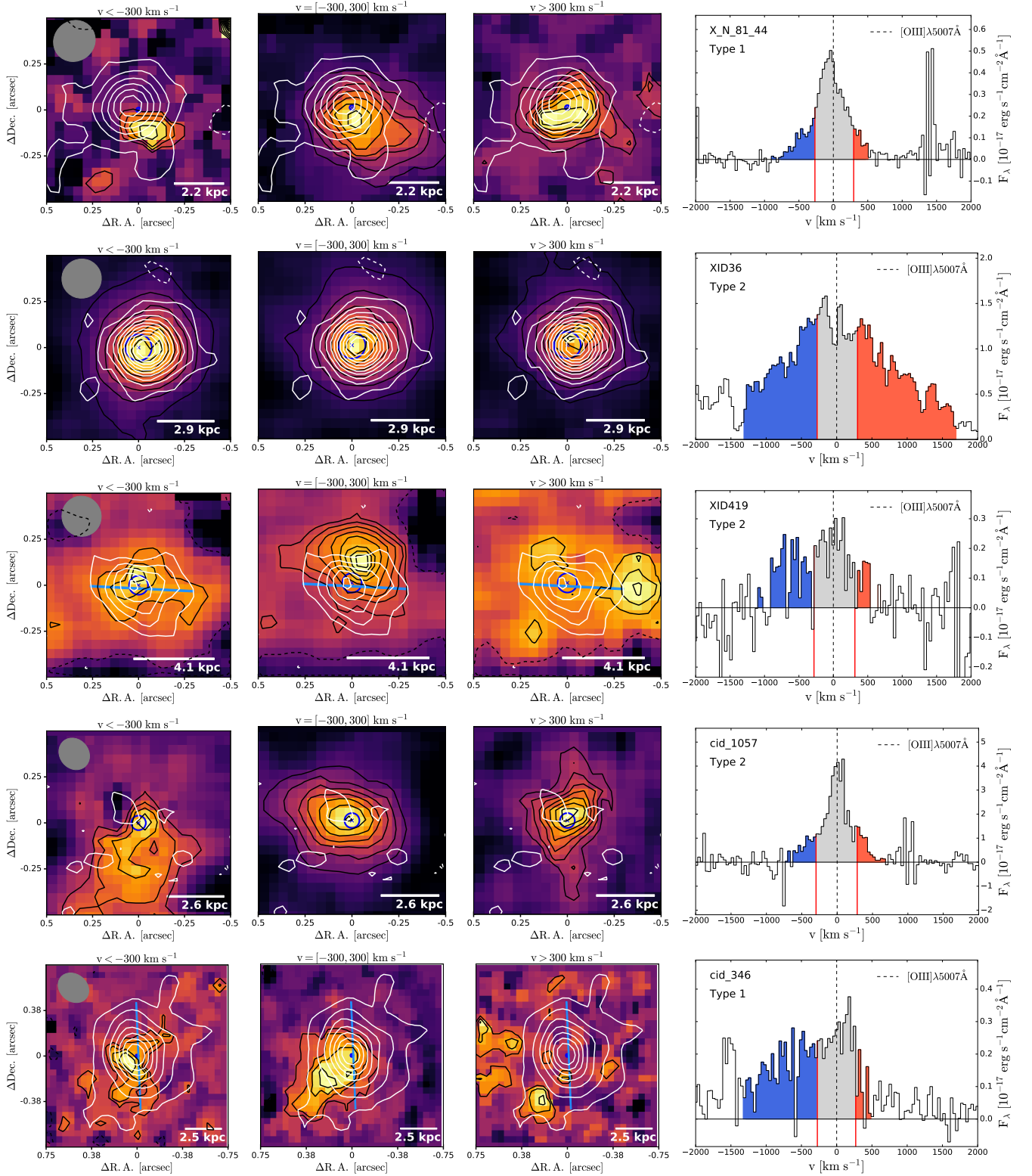


Fig. 10. Maps of [O III] emission in three different velocity channels: blue-shifted emission ($<-300 \text{ km s}^{-1}$, *first column*), central channel ($[-300, 300] \text{ km s}^{-1}$, *second column*), red-shifted emission ($>300 \text{ km s}^{-1}$, *third column*). The interval over which the spectrum has been integrated is indicated on the right plot. In black are the [O III] emission contours starting from 2σ and increasing in intervals of 1σ (and in intervals of 2σ for XID36, cid_451 and cid_1143, to improve presentation). In white are the FIR emission contours, starting from 2σ and increasing in intervals of 2σ (or intervals of 4σ for X_N_81_44 and cid_346, to improve presentation). Negative -2σ contours are shown with dashed curves. The grey ellipse shows the size of the ALMA beam, while the white scale-bar shows the size of the PSF of the [O III] image in kpc. The blue cross and circle show the position and uncertainty of the optical continuum. The lightblue bar indicates the position angle along the major axis of the FIR emission, when it can be reliably determined (see Sect. 3.3.1). *Fourth column*: spectrum around the [O III] $\lambda 5007 \text{ \AA}$ emission line. The coloured areas show the spectral regions over which the emission was integrated to create the three images on the left.

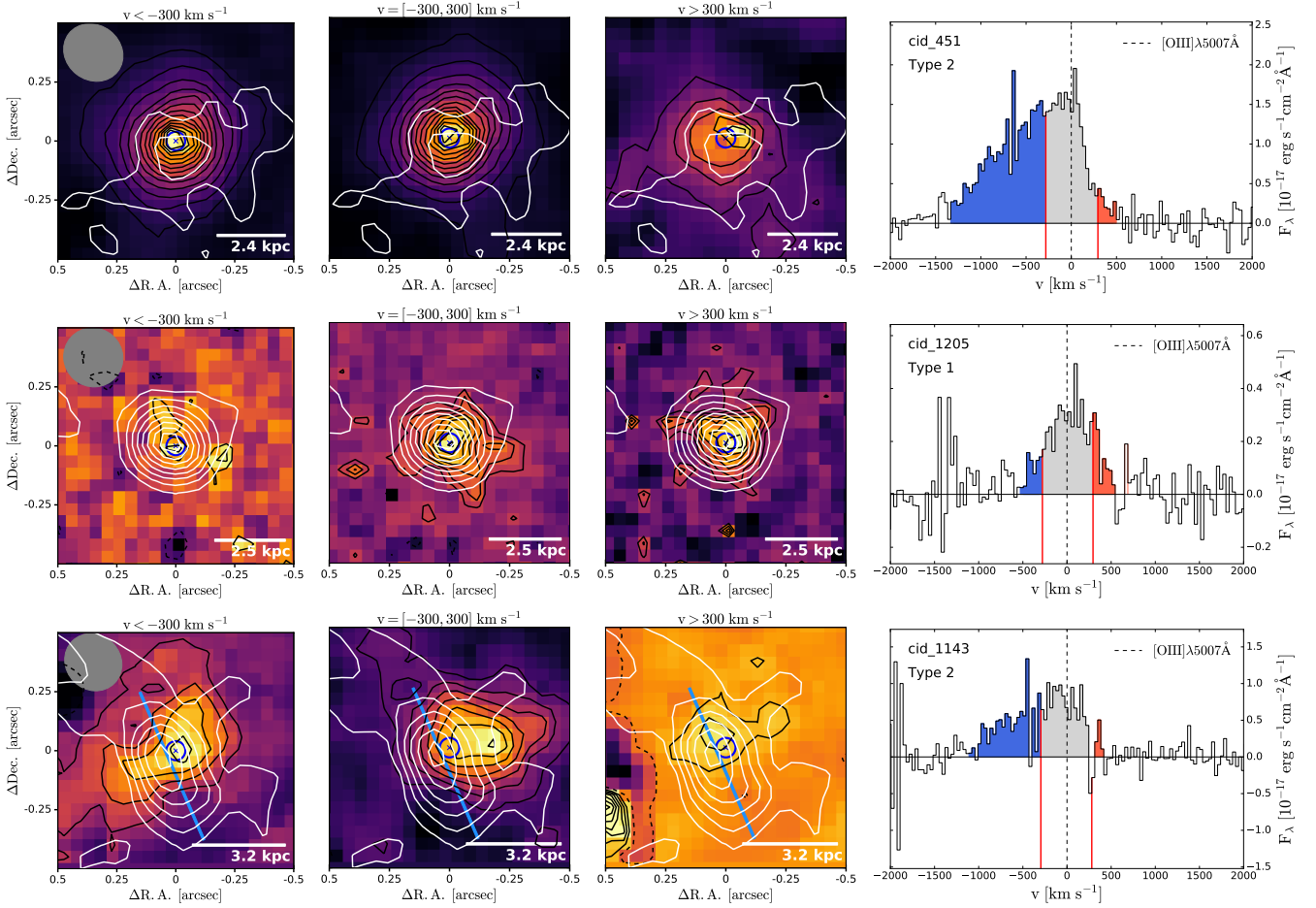


Fig. 10. continued.

of the FIR emission. If the stellar disk is oriented as the dust emission, this may suggest that the outflow is moving along the path of least resistance, which is perpendicular to the disk (Gabor & Bournaud 2014).

Under the assumption that the FIR emission is a reliable tracer of the SFR, we do not see evidence that the obscured star formation is suppressed or disturbed in the location of the outflow. We discuss this result further in the next section.

5.5. Implications of our results

The main goal of this study is to trace with high spatial resolution the star formation in the host galaxies of AGN with powerful outflows, to assess the impact that these may have on the mass build-up of the galaxies.

Since our targets are powerful AGN, we expected the $H\alpha$ maps to be contaminated by AGN emission. Our BPT analysis confirms that for all but one target (cid_346) the $H\alpha$ emission is AGN dominated. Thus, we cannot use $H\alpha$ as a star formation tracer in our sample and we have to rely only on the FIR, which traces obscured star formation.

In this study, we use the monochromatic FIR emission at $\sim 260\mu\text{m}$ to trace obscured star formation. This relies on the assumption that spatial variations of the shape of the FIR SED (due to changes in the dust properties, as for example the dust temperature and emissivity index β) are negligible. Under this assumption, the single FIR image can be translated into a map of the FIR luminosity and, consequently, of the obscured SFR. In

order to test how spatial variations in the dust temperature may affect our results, we would need spatially resolved FIR observations at other wavelengths.

As described Sect. 5.4, we do not find any evidence of the ionised outflows instantaneously regulating the star formation in their host galaxies, for example, through cavities or ‘holes’ in the FIR emission. Similar results are reported by Balmaverde et al. (2016), who study a sample of quasars at $z < 1$ and find that quasars with strong outflows do not show lower SFR than those with weaker outflows. Other spatially-resolved studies of AGN at $z \sim 1.4\text{--}2.6$ also find no evidence of instantaneous star formation suppression due to the ionised outflows (Scholtz et al. 2020, 2021).

When looking for evidence of AGN feedback on star formation, we need to consider the timescales of the star formation tracer we are using. If the impact of the AGN on the level of star formation is on short timescales, then a star formation rate tracer too sensitive to the past star formation history of the galaxy may dilute the feedback signature. The FIR is commonly believed to trace star formation on timescales of $\sim 100\text{Myr}$. However, some studies find no significant difference in the SFR measured from the FIR and from $H\alpha$ in star-forming galaxies (e.g. Lam et al. 2013; Dominguez-Sanchez et al. 2014; Rosario et al. 2016), which is believed to measure SFR on shorter timescales ($\sim 10\text{Myr}$). This would suggest that the FIR traces similar star formation timescales as the $H\alpha$ emission. However, this result may depend on the star formation history of the individual galaxies. In this context, it would then be very interesting to

have an alternative and reliable tracer of the star formation on short timescales. Standing the limitations of using $H\alpha$ or the UV emission for AGN hosts, an alternative could be to use the mid-infrared PAHs features which would be accessible at these redshifts with JWST.

On the other hand, it is also possible that the outflow needs some time to produce an effect on the star formation. Thus, there is a delay between the moment the outflow is visible and when the star formation decreases. Episodes of AGN activity happen on shorter timescales compared to timescales of star formation variations (Gabor & Bournaud 2014; Hickox et al. 2014). The outflow may need more time to remove a substantial quantity of gas from the host galaxy and cause a suppression of star formation. Simulations by Gabor & Bournaud (2014) show that AGN-driven outflows do not cause instantaneous quenching, but they may remove a substantial amount of gas on long timescales (\gtrsim Gyr). Recently, Costa et al. (2020) found that AGN feedback acts in two modes in their simulations: a rapid mode that removes dense gas from the nucleus, and a slower mode that prevents halo gas accretion. The first mode alone will not cause a decrease in the star formation, but the combination of the two modes will suppress star formation in the long-term. Some observations show that high-redshift AGN host galaxies may have lower molecular gas fractions, the fuel for star formation, compared to mass-matched star-forming galaxies at high redshift (e.g. Kakkad et al. 2017; Circosta et al. 2021). Over time, this should be visible as an impact on the star formation itself.

Moreover, we need to consider also the physical scales that we are sampling in this study. We do not see signs of star formation suppression at the scales probed by our observations (≥ 2 kpc), but it is possible that the impact of the outflows is only visible at smaller scales. Outflows may influence star formation only in a small region of the galaxy, on scale < 1 kpc (e.g. Croft et al. 2006; Alatalo et al. 2015; Cresci et al. 2015b; Querejeta et al. 2016; Rosario et al. 2019; Shin et al. 2019; Husemann et al. 2019).

There is also the possibility that the interaction between the outflow and the ISM is limited. We observe that, at least in two targets (cid_346 and cid_1143), the ionised gas is located preferentially perpendicular to the dust. This may indicate that the outflow is propagating following the path of least resistance. Simulations have shown that AGN-driven outflows propagate preferably away from the plane of the galaxy, avoiding dense gas regions in the galactic disk (Gabor & Bournaud 2014; Costa et al. 2014; Mukherjee et al. 2016).

To interpret our results, we also need to consider how representative of the parent population our sample is. Due to the requirement to have FIR detections, our targets tend to have higher SFRs compared to the average of the parent SUPER sample, in which there are many SFR upper limits (see Fig. 1). Additionally, our sample has a higher SSFR compared to the average of the parent population of X-ray AGN at $z \sim 2$ (Scholtz et al. 2018). It is possible that if we were to target AGN with lower SFRs, we would be more likely to observe localised suppression of star formation, since the total star formation level is lower. To test this hypothesis, it would require deep ALMA continuum observations to get spatially resolved maps of the dust continuum emission for the whole SUPER sample.

6. Summary and conclusions

We present ALMA Band 7 observed-frame 870 μm (rest-frame $\sim 260 \mu\text{m}$) continuum high-resolution ($\sim 0.2''$, corresponding to ~ 2 kpc) observations of eight X-ray AGN at redshift $z \sim 2$ from

the SUPER sample. The ALMA targets were selected from the parent SUPER sample based on photometric detections in the FIR (i.e. observed wavelength 24–870 μm) and [O III] detections in the SINFONI IFS maps. The selected sample has a range of bolometric luminosities which is representative of the parent sample ($L_{\text{bol}} = 10^{44.9} - 10^{46.8} \text{ erg s}^{-1}$). They have SFRs in the range 8–380 $M_{\odot} \text{ yr}^{-1}$ and most of the targets lie near the star formation main-sequence, with the exception of cid_1143 that lies below (see Fig. 1). The main conclusions of this work are:

- We detect 6/8 of our targets with $S/N > 8$ in the ALMA rest-frame 260 μm continuum maps. The rest of the conclusions are based on these six high S/N targets. We model the 260 μm data in the visibilities versus uv -distance space using different models (point source, Gaussian, exponential profile, Gaussian+point source). From the ‘best fit’ models, we measure flux densities in the range 0.27–2.58 mJy and half-light radii in the range $R_e = 0.83 - 2.01$ kpc (median 1.31 ± 0.23 kpc) (Sect. 3.3).
- From the SED decomposition, we find that the contribution of AGN-heated dust to the total rest-frame 260 μm emission is $\leq 4\%$ in our sample. The contribution from synchrotron emission from AGN is small in most of the targets ($< 1\%$). We conclude that the main contribution to the 260 μm flux is due to dust heated by star formation (see Sect. 5.1).
- We compare the FIR sizes of our sample with other samples of SFGs and AGN at similar redshift, for which the FIR sizes are measured from ALMA (observed-frame) 870 μm observations of similar resolution and sensitivity (see Sect. 5.2, Fig. 6). Our sample is in agreement with literature samples of redshift-matched star-forming and AGN host galaxies. Across these samples, we find that the mean FIR size of AGN ($R_e = 1.16 \pm 0.11$ kpc) is smaller than the mean FIR size of non-AGN ($R_e = 1.69 \pm 0.13$ kpc). A possible interpretation is that a compact dust/gas configuration favours the accretion to the central SMBH.
- We use the redshift-dependent BPT diagnostic diagram from Kewley et al. (2013a,b) to identify the main process responsible for gas ionisation in our sample (Fig. 7). Most of our objects lie in the AGN region, with the exception of cid_346 (see Sect. 5.3.1). We find a good agreement between the spatial distribution of $H\alpha$ and [O III] in most of the targets (see Sect. 5.3.2, Fig. 3). This suggests that the same mechanism responsible for the [O III] emission, that is the AGN, is also partly responsible for the $H\alpha$ emission. Only two objects (X_N_81_44 and cid_346) show a significant offset between the peak of $H\alpha$ and [O III] emission, which could be a sign that there are different contributions from the ionisation sources or it could be due to differential obscuration. In summary, across our sample we do not identify any $H\alpha$ emission that we can confidently use to trace star formation.
- We observe different spatial distributions of ionised gas and FIR emission (Figs. 3 and 8). Specifically, in most of our targets (4/6) there is a significant offset between the central position of the ionised gas emission and the FIR emission (0.4–1.9 kpc). We also find that the ionised gas emission tends to be larger than the FIR emission by a factor of ~ 1.7 (Fig. 9). Most strikingly, in two sources (cid_1143 and cid_346) we observe that the ionised gas is perpendicular to the dust emission. All of these observations provides further evidence that dust and ionised gas emission are not directly associated in our sample, with the dust most likely to be tracing the host galaxy and the ionised gas most likely to be tracing the AGN emission-line regions.

– Comparing the position of the [O III] blue-shifted emission with the FIR emission (Fig. 10), we find that the FIR emission is unaffected by the ionised outflow. Assuming that the FIR is tracing the obscured star formation, we see no evidence for star formation suppression due to the ionised outflows at the scale probed by our observations (~ 2 kpc). However, we do not have a resolved map of an alternative and reliable tracer of only recent star formation. Additionally, the outflow may need longer timescales to significantly affect star formation. In at least two objects (cid_346 and cid_1143), the outflow is almost perpendicular to the direction of the major axis of the FIR emission, which can be an indication that the outflow propagates following the path of least resistance.

We do not observe any evidence in this study for ionised outflows directly influencing star formation. However, one limitation is that our sample may be biased to relatively high SFRs. To confirm that the ionised outflows do not have an impact on star formation, we need to obtain spatially-resolved FIR maps also for the SUPER targets with lower SFRs. Furthermore, future IFS observations with higher spatial resolution (e.g. with ELT/HARMONI) will help to get spatially-resolved emission-line ratio diagnostics that will allow us to map and identify the ionisation sources of $H\alpha$ in a spatially-resolved way.

Acknowledgements. We thank the anonymous referee for carefully reading the paper and providing constructive comments. We thank Ian Smail and Bitten Gullberg for helping us to understand the data of the AS2UDS sample. I.L. acknowledges support from the Comunidad de Madrid through the Atracción de Talento Investigador Grant 2018-T1/TIC-11035. M.P. is supported by the Programa Atracción de Talento de la Comunidad de Madrid via grant 2018-T2/TIC-11715. C.C.C. acknowledges support from the Ministry of Science and Technology of Taiwan (MOST 109-2112-M-001-016-MY3). D.M.A. and D.J.R. acknowledge support from STFC (ST/T000244/1). A.P. gratefully acknowledges financial support from STFC through grants ST/T000244/1 and ST/P000541/1. G.V. acknowledges financial support from Premiale 2015 MITic (PI B. Garilli). This paper is based on observations collected at the European organisation for Astronomical Research in the Southern Hemisphere under ESO programme 196.A-0377. This paper makes use of the following ALMA data: ADS/JAO.ALMA#2018.1.00992.S. ALMA is a partnership of ESO (representing its member states), NSF (USA) and NINS (Japan), together with NRC (Canada), MOST and ASIAA (Taiwan), and KASI (Republic of Korea), in cooperation with the Republic of Chile. The Joint ALMA Observatory is operated by ESO, AUI/NRAO and NAOJ. Based in part on data products produced by TERAPIX and the Cambridge Astronomy Survey Unit on behalf of the UltraVISTA consortium. Based on observations obtained as part of the VISTA Hemisphere Survey, ESO Program, 179.A-2010 (PI: McMahon). This work has made use of data from the European Space Agency (ESA) mission *Gaia* (<https://www.cosmos.esa.int/gaia>), processed by the *Gaia* Data Processing and Analysis Consortium (DPAC, <https://www.cosmos.esa.int/web/gaia/dpac/consortium>). Funding for the DPAC has been provided by national institutions, in particular the institutions participating in the *Gaia* Multilateral Agreement. The Starlink software (Currie et al. 2014) is currently supported by the East Asian Observatory. This research has made use of the NASA/IPAC Extragalactic Database (NED) which is operated by the Jet Propulsion Laboratory, California Institute of Technology, under contract with the National Aeronautics and Space Administration. This research made use of Astropy, a community-developed core Python package for Astronomy (Astropy Collaboration 2013), Matplotlib (Hunter 2007) and NumPy (Van Der Walt et al. 2011). This research used the TOPCAT tool for catalogue cross-matching (Taylor 2005), the Stan interface for Python PyStan (Stan Development Team 2018), and APLpy, an open-source plotting package for Python (Robitaille & Bressert 2012).

References

- Aird, J., Coil, A. L., & Georgakakis, A. 2017, *MNRAS*, 465, 3390
- Akaike, H. 1973, in *Information Theory and an Extension of the Maximum Likelihood Principle*, eds. B. N. Petrov, & F. Csaki (Budapest: Akademiai Kiado), 2nd Int. Symp. Inf. Theor., 267
- Akaike, H. 1974, *IEEE Trans. Autom. Control*, 19, 716
- Alatalo, K., Lacy, M., Lanz, L., et al. 2015, *ApJ*, 798, 31
- Astropy Collaboration (Robitaille, T. P., et al.) 2013, *A&A*, 558, A33
- Bae, H.-J., & Woo, J.-H. 2016, *ApJ*, 828, 97
- Baldwin, J. A., Phillips, M. M., & Terlevich, R. 1981, *PASP*, 93, 5
- Balmaverde, B., Marconi, A., Brusa, M., et al. 2016, *A&A*, 585, A148
- Barro, G., Kriek, M., Pérez-González, P. G., et al. 2016, *ApJ*, 827, L32
- Becker, R. H., White, R. L., & Helfand, D. J. 1995, *ApJ*, 450, 559
- Behroozi, P. S., Wechsler, R. H., & Conroy, C. 2013, *ApJ*, 770, 57
- Bolzoniella, M., Kovac, K., Pozzetti, L., et al. 2010, *A&A*, 524, A76
- Boquien, M., Burgarella, D., Roehly, Y., et al. 2019, *A&A*, 622, A103
- Boroson, T. A., & Green, R. F. 1992, *ApJS*, 80, 109
- Bouwens, R., González-López, J., Aravena, M., et al. 2020, *ApJ*, 902, 112
- Brinchmann, J., Charlot, S., White, S. D. M., et al. 2004, *MNRAS*, 351, 1151
- Brusa, M., Cresci, G., Daddi, E., et al. 2018, *A&A*, 612, A29
- Burgarella, D., Buat, V., & Iglesias-Páramo, J. 2005, *MNRAS*, 360, 1413
- Calistro Rivera, G., Lusso, E., Hennawi, J. F., & Hogg, D. W. 2016, *ApJ*, 833, 98
- Calistro Rivera, G., Hodge, J. A., Smail, I., et al. 2018, *ApJ*, 863, 56
- Cano-Díaz, M., Maiolino, R., Marconi, A., et al. 2012, *A&A*, 537, L8
- Carniani, S., Marconi, A., Maiolino, R., et al. 2016, *A&A*, 591, A28
- Carpenter, B., Gelman, A., Hoffman, M. D., et al. 2017, *J. Stat. Softw. Artic.*, 76, 1
- Casey, C. M., Narayanan, D., & Cooray, A. 2014, *Phys. Rep.*, 541, 45
- Chabrier, G. 2003, *PASP*, 115, 763
- Chang, Y.-Y., Le Floch, E., Juneau, S., et al. 2020, *ApJ*, 888, 44
- Chen, C.-C., Smail, I., Swinbank, A. M., et al. 2015, *ApJ*, 799, 194
- Chen, C.-C., Hodge, J. A., Smail, I., et al. 2017, *ApJ*, 846, 108
- Chen, C.-C., Harrison, C. M., Smail, I., et al. 2020, *A&A*, 635, A119
- Cheng, C., Ibar, E., Smail, I., et al. 2020, *MNRAS*, 499, 5241
- Choi, E., Somerville, R. S., Ostriker, J. P., Naab, T., & Hirschmann, M. 2018, *ApJ*, 866, 91
- Cicone, C., Brusa, M., Ramos Almeida, C., et al. 2018, *Nat. Astron.*, 2, 176
- Circosta, C., Mainieri, V., Padovani, P., et al. 2018, *A&A*, 620, A82
- Circosta, C., Mainieri, V., Lamperti, I., et al. 2021, *A&A*, 646, A96
- Civano, F., Marchesi, S., Comastri, A., et al. 2016, *ApJ*, 819, 62
- Condon, J. J. 1997, *PASP*, 109, 166
- Costa, T., Sijacki, D., & Haehnelt, M. G. 2014, *MNRAS*, 444, 2355
- Costa, T., Pakmor, R., & Springel, V. 2020, *MNRAS*, 497, 5229
- Crenshaw, D. M., Schmitt, H. R., Kraemer, S. B., Mushotzky, R. F., & Dunn, J. P. 2010, *ApJ*, 708, 419
- Cresci, G., & Maiolino, R. 2018, *Nat. Astron.*, 2, 179
- Cresci, G., Mainieri, V., Brusa, M., et al. 2015a, *ApJ*, 799, 82
- Cresci, G., Marconi, A., Zibetti, S., et al. 2015b, *A&A*, 582, A63
- Croft, S., van Breugel, W., de Vries, W., et al. 2006, *ApJ*, 647, 1040
- Currie, M. J., Berry, D. S., Jenness, T., et al. 2014, *ASP Conf. Ser.*, 485, 391
- D'Agostino, J. J., Kewley, L. J., Groves, B. A., et al. 2019, *MNRAS*, 485, L38
- Dale, D. A., Helou, G., Magdis, G. E., et al. 2014, *ApJ*, 784, 83
- Dicken, D., Tadhunter, C., Morganti, R., et al. 2008, *ApJ*, 678, 712
- Di Mascia, F., Gallerani, S., Behrens, C., et al. 2021, *MNRAS*, 503, 2349
- Dominguez-Sanchez, H., Bongiovanni, A., Lara-López, M. A., et al. 2014, *MNRAS*, 441, 2
- Donley, J. L., Koekemoer, A. M., Brusa, M., et al. 2012, *ApJ*, 748, 142
- Duras, F., Bongiorno, A., Piconcelli, E., et al. 2017, *A&A*, 604, A67
- Elbaz, D., Daddi, E., Le Borgne, D., et al. 2007, *A&A*, 468, 33
- Elbaz, D., Leiton, R., Nagar, N., et al. 2018, *A&A*, 616, A110
- Fabian, A. C. 2012, *ARA&A*, 50, 455
- Falkendal, T., De Breuck, C., Lehnert, M. D., et al. 2019, *A&A*, 621, A27
- Feruglio, C., Fiore, F., Carniani, S., et al. 2015, *A&A*, 583, A99
- Förster Schreiber, N. M., Renzini, A., Mancini, C., et al. 2018, *ApJS*, 238, 21
- Fritz, J., Franceschini, A., & Hatziminaoglou, E. 2006, *MNRAS*, 366, 767
- Fujimoto, S., Ouchi, M., Shibuya, T., & Nagai, H. 2017, *ApJ*, 850, 83
- Fujimoto, S., Ouchi, M., Kohno, K., et al. 2018, *ApJ*, 861, 7
- Gabor, J. M., & Bournaud, F. 2014, *MNRAS*, 441, 1615
- Gaia Collaboration (Prusti, T., et al.) 2016, *A&A*, 595, A1
- Gaia Collaboration (Brown, A. G. A., et al.) 2018, *A&A*, 616, A1
- Gallagher, R., Maiolino, R., Belfiore, F., et al. 2019, *MNRAS*, 485, 3409
- Grimmett, L. P., Mullaney, J. R., Bernhard, E. P., et al. 2020, *MNRAS*, 495, 1392
- Gullberg, B., Smail, I., Swinbank, A. M., et al. 2019, *MNRAS*, 490, 4956
- Harrison, C. M. 2017, *Nat. Astron.*, 1, 0165
- Harrison, C. M., Simpson, J. M., Stanley, F., et al. 2016a, *MNRAS*, 457, L122
- Harrison, C. M., Alexander, D. M., Mullaney, J. R., et al. 2016b, *MNRAS*, 456, 1195
- Hickox, R. C., Mullaney, J. R., Alexander, D. M., et al. 2014, *ApJ*, 782, 9
- Hodge, J. A., Karim, A., Smail, I., et al. 2013, *ApJ*, 768, 91
- Hodge, J. A., Swinbank, A. M., Simpson, J. M., et al. 2016, *ApJ*, 833, 103
- Hunter, J. D. 2007, *Comput. Sci. Eng.*, 9, 90
- Husemann, B., Scharwächter, J., Davis, T. A., et al. 2019, *A&A*, 627, A53
- Huyhn, M. T., Hopkins, A. M., Lenc, E., et al. 2012, *MNRAS*, 426, 2342
- Ikarashi, S., Ivison, R. J., Caputi, K. I., et al. 2015, *ApJ*, 810, 133
- Ishibashi, W., & Fabian, A. C. 2016, *MNRAS*, 457, 2864

- Jarvis, M. E., Harrison, C. M., Thomson, A. P., et al. 2019, *MNRAS*, **485**, 2710
- Kakkad, D., Mainieri, V., Padovani, P., et al. 2016, *A&A*, **592**, A148
- Kakkad, D., Mainieri, V., Brusa, M., et al. 2017, *MNRAS*, **468**, 4205
- Kakkad, D., Mainieri, V., Vietri, G., et al. 2020, *A&A*, **642**, A147
- Karim, A., Swinbank, A. M., Hodge, J. A., et al. 2013, *MNRAS*, **432**, 2
- Kauffmann, G., Heckman, T. M., Tremonti, C., et al. 2003, *MNRAS*, **346**, 1055
- Kennicutt, R. C., Jr. 1998, *ApJ*, **498**, 541
- Kennicutt, R. C., & Evans, N. J. 2012, *ARA&A*, **50**, 531
- Kewley, L. J., Dopita, M. A., Leitherer, C., et al. 2013a, *ApJ*, **774**, 100
- Kewley, L. J., Maier, C., Yabe, K., et al. 2013b, *ApJ*, **774**, L10
- King, A. 2003, *ApJ*, **596**, L27
- King, A., & Pounds, K. 2015, *ARA&A*, **53**, 115
- Kocevski, D. D., Hasinger, G., Brightman, M., et al. 2018, *ApJS*, **236**, 48
- Lacy, M. I., Storrie-Lombardi, L. J., Sajina, A., et al. 2004, *ApJS*, **154**, 166
- Lam, M. T., Wu, H., Zhu, Y.-N., & Zhou, Z.-M. 2013, *Res. Astron. Astrophys.*, **13**, 179
- Lang, P., Schinnerer, E., Smail, I., et al. 2019, *ApJ*, **879**, 54
- Lani, C., Netzer, H., & Lutz, D. 2017, *MNRAS*, **471**, 59
- Luo, B., Brandt, W. N., Xue, Y. Q., et al. 2017, *ApJS*, **228**, 2
- Lutz, D., Shimizu, T., Davies, R. I., et al. 2018, *A&A*, **609**, A9
- Madau, P., & Dickinson, M. 2014, *ARA&A*, **52**, 415
- Madau, P., Ferguson, H. C., Dickinson, M. E., et al. 1996, *MNRAS*, **283**, 1388
- Mainieri, V., Bergeron, J., Hasinger, G., et al. 2002, *A&A*, **393**, 425
- Maiolino, R., Russell, H. R., Fabian, A. C., et al. 2017, *Nature*, **544**, 202
- Mancini, C., Förster Schreiber, N. M., Renzini, A., et al. 2011, *ApJ*, **743**, 86
- Marasco, A., Cresci, G., Nardini, E., et al. 2020, *A&A*, **644**, A15
- Marchesi, S., Civano, F., Elvis, M., et al. 2016, *ApJ*, **817**, 34
- Marconi, A., Risaliti, G., Gilli, R., et al. 2004, *MNRAS*, **351**, 169
- McCracken, H. J., Milvang-Jensen, B., Dunlop, J., et al. 2012, *A&A*, **544**, A156
- McElroy, R. E., Husemann, B., Croom, S. M., et al. 2016, *A&A*, **593**, L8
- McKinney, J., Hayward, C. C., Rosenthal, L. J., et al. 2021, *ApJ*, submitted [arXiv:2103.12747]
- McMahon, R. G., Banerji, M., Gonzalez, E., et al. 2013, *The Messenger*, **154**, 35
- Miller, N. A., Bonzini, M., Fomalont, E. B., et al. 2013, *ApJS*, **205**, 13
- Mukherjee, D., Bicknell, G. V., Sutherland, R., & Wagner, A. 2016, *MNRAS*, **461**, 1967
- Mukherjee, D., Bicknell, G. V., Wagner, A. Y., Sutherland, R. S., & Silk, J. 2018, *MNRAS*, **479**, 5544
- Mullaney, J. R., Alexander, D. M., Goulding, A. D., & Hickox, R. C. 2011, *MNRAS*, **414**, 1082
- Mullaney, J. R., Alexander, D. M., Aird, J., et al. 2015, *MNRAS*, **453**, L83
- Ni, Q., Brandt, W. N., Yang, G., et al. 2021, *MNRAS*, **500**, 4989
- Noll, S., Burgarella, D., Giovannoli, E., et al. 2009, *A&A*, **507**, 1793
- Osterbrock, D. E., & Ferland, G. J. 2006, *Astrophysics of Gaseous Nebulae and Active Galactic Nuclei* (Sausalito: University Science Books)
- Perna, M., Cresci, G., Brusa, M., et al. 2019, *A&A*, **623**, A171
- Perna, M., Arribas, S., Catalan-Torrecilla, C., et al. 2020, *A&A*, **643**, A139
- Pier, E. A., & Krolik, J. H. 1992, *ApJ*, **401**, 99
- Pierre, M., Pacaud, F., Adami, C., et al. 2016, *A&A*, **592**, A1
- Popping, G., Pillepich, A., Calistro Rivera, G., et al. 2021, *MNRAS*, submitted [arXiv:2101.12218]
- Puglisi, A., Daddi, E., Renzini, A., et al. 2017, *ApJ*, **838**, L18
- Puglisi, A., Daddi, E., Liu, D., et al. 2019, *ApJ*, **877**, L23
- Querejeta, M., Schinnerer, E., García-Burillo, S., et al. 2016, *A&A*, **593**, A118
- Retzlaff, J., Rosati, P., Dickinson, M., et al. 2010, *A&A*, **511**, A50
- Robitaille, T., & Bressert, E. 2012, *Astrophysics Source Code Library* [record ascl:1208.017]
- Rosario, D. J., Mendel, J. T., Ellison, S. L., Lutz, D., & Trump, J. R. 2016, *MNRAS*, **457**, 2703
- Rosario, D. J., Togi, A., Burtscher, L., et al. 2019, *ApJ*, **875**, L8
- Rupke, D. S. N., Gültekin, K., & Veilleux, S. 2017, *ApJ*, **850**, 40
- Salpeter, E. E. 1955, *ApJ*, **121**, 161
- Santini, P., Ferguson, H. C., Fontana, A., et al. 2015, *ApJ*, **801**, 97
- Schinnerer, E., Smolčić, V., Carilli, C. L., et al. 2007, *ApJS*, **172**, 46
- Schneider, R., Bianchi, S., Valiante, R., Risaliti, G., & Salvadori, S. 2015, *A&A*, **579**, A60
- Scholtz, J., Alexander, D. M., Harrison, C. M., et al. 2018, *MNRAS*, **475**, 1288
- Scholtz, J., Harrison, C. M., Rosario, D. J., et al. 2020, *MNRAS*, **492**, 3194
- Scholtz, J., Harrison, C. M., Rosario, D. J., et al. 2021, *MNRAS*, **505**, 5469
- Schreiber, C., Pannella, M., Elbaz, D., et al. 2015, *A&A*, **575**, A74
- Schwarz, G. 1978, *Ann. Stat.*, **6**, 461
- Shankar, F., Weinberg, D. H., & Miralda-Escudé, J. 2009, *ApJ*, **690**, 20
- Shapiro, S. L., Teukolsky, S. A., & Lightman, A. P. 1983, *Phys. Today*, **36**, 89
- Shin, J., Woo, J.-H., Chung, A., et al. 2019, *ApJ*, **881**, 147
- Silva, L., Granato, G. L., Bressan, A., & Danese, L. 1998, *ApJ*, **509**, 103
- Simpson, J. M., Smail, I., Swinbank, A. M., et al. 2015, *ApJ*, **799**, 81
- Smolčić, V., Novak, M., Bondi, M., et al. 2017, *A&A*, **602**, A1
- Somerville, R. S., Hopkins, P. F., Cox, T. J., Robertson, B. E., & Hernquist, L. 2008, *MNRAS*, **391**, 481
- Stacey, H. R., McKean, J. P., Powell, D. M., et al. 2021, *MNRAS*, **500**, 3667
- Stach, S. M., Dudzevičiūtė, U., Smail, I., et al. 2019, *MNRAS*, **487**, 4648
- Stan Development Team 2018, *PyStan: the Python Interface to Stan, Version 2.17.1.0*
- Stanley, F., Harrison, C. M., Alexander, D. M., et al. 2018, *MNRAS*, **478**, 3721
- Stern, D., Assef, R. J., Benford, D. J., et al. 2012, *ApJ*, **753**, 30
- Storchi-Bergmann, T., Lopes, R. D. S., McGregor, P. J., et al. 2010, *MNRAS*, **402**, 819
- Szokoly, G. P., Bergeron, J., Hasinger, G., et al. 2004, *ApJS*, **155**, 271
- Tacconi, L. J., Genzel, R., & Sternberg, A. 2020, *ARA&A*, **58**, 157
- Tadaki, K.-I., Genzel, R., Kodama, T., et al. 2017, *ApJ*, **834**, 135
- Tadaki, K.-I., Belli, S., Burkert, A., et al. 2020, *ApJ*, **901**, 74
- Taylor, M. B. 2005, *ASP Conf. Ser.*, **347**, 29
- Trayford, J. W., Theuns, T., Bower, R. G., et al. 2016, *MNRAS*, **460**, 3925
- Tsuzuki, Y., Kawara, K., Yoshii, Y., et al. 2006, *ApJ*, **650**, 57
- Van Der Walt, S., Colbert, S. C., & Varoquaux, G. 2011, *Comput. Sci. Eng.*, **13**, 22
- Veilleux, S., Meléndez, M., Sturm, E., et al. 2013, *ApJ*, **776**, 27
- Venturi, G., Marconi, A., Mingozzi, M., et al. 2017, *Front. Astron. Space Sci.*, **4**, 46
- Venturi, G., Nardini, E., Marconi, A., et al. 2018, *A&A*, **619**, A74
- Veron-Cetty, M. P., Joly, M., & Veron, P. 2004, *A&A*, **417**, 515
- Viaene, S., Nersesian, A., Fritz, J., et al. 2020, *A&A*, **638**, A150
- Vietri, G., Piconcelli, E., Bischetti, M., et al. 2018, *A&A*, **617**, A81
- Vietri, G., Mainieri, V., Kakkad, D., et al. 2020, *A&A*, **644**, A175
- Wang, S. X., Brandt, W. N., Luo, B., et al. 2013, *ApJ*, **778**, 179
- Whitaker, K. E., Rigby, J. R., Brammer, G. B., et al. 2014, *ApJ*, **790**, 143
- Zubovas, K. 2018, *MNRAS*, **479**, 3189

Appendix A: Models used to fit the FIR profile

Table A.1. Range of priors used for the fit of the visibilities vs. uv -distances. F is the flux density and σ_{uv} is the scale parameter.

Model	parameter	priors
point	F	0 – 1000 mJy
Gaussian	F	0 – 1000 mJy
	σ_{uv}	0 – 10000 k λ
Gaussian+point	$F(\text{Gauss})$	0 – 5 mJy
	σ_{uv}	0 – 10000 k λ
	$F(\text{point})$	0 – 5 mJy
exponential	F	0 – 1000 mJy
	σ_{uv}	0 – 20000 k λ

To assess the morphology of the FIR emission, we fit the visibilities versus uv -distances using the following models: point source, Gaussian, Gaussian+point source, and exponential profile. We Fourier-transformed the models to perform the fit in the visibilities versus uv -distance plane. The models in the visibilities versus uv -distance plane are defined as:

- *Point source*: a point source is represented as a constant model as a function of uv -distance:

$$f(x, F) = F, \quad (\text{A.1})$$

where F is the flux density in mJy and x is the uv -distance in units of k λ , where λ is the wavelength of the observation.

- *Gaussian profile*: the Fourier transform of a Gaussian model is also a Gaussian defined as:

$$f(x, F, \sigma_{uv}) = F \cdot \exp\left(-\frac{1}{2} \left(\frac{x}{\sigma_{uv}}\right)^2\right), \quad (\text{A.2})$$

where F is the flux density in mJy and σ_{uv} is the scale parameter. σ_{uv} is related to the effective radius R_e (in radians) as:

$$R_e[\text{rad}] = \frac{FWHM}{2} = \frac{2.355}{2} \cdot \sigma = \frac{2.355}{2} \cdot \frac{1}{2\pi\sigma_{uv} \cdot 10^3}, \quad (\text{A.3})$$

where the factor 10^3 is necessary to convert from k λ to λ . The effective radius in arcsec is obtained as $R_e[\text{arcsec}] = R_e[\text{rad}] \frac{180 \cdot 3600}{\pi}$.

- *Gaussian+point source*: this model combines the previous two models:

$$f(x, F_{Gauss.}, \sigma_{uv}, F_{point}) = f_{Gauss.}(x, F_{Gauss.}, \sigma_{uv}) + F_{point}, \quad (\text{A.4})$$

where $F_{Gauss.}$ and F_{point} are the flux densities of the Gaussian and point source components, respectively. The total flux density is given by $F(\text{tot}) = F_{Gauss.} + F_{point}$.

- *Exponential profile*: the exponential profile is modelled as:

$$f(x, F, \sigma_{uv}) = F \cdot \frac{\sigma_{uv}}{\sigma_{uv}^2 + x^2}, \quad (\text{A.5})$$

where σ_{uv} is related to the effective radius R_e (in radians) as:

$$R_e[\text{rad}] = 1.6783 \cdot \sigma = 1.6783 \cdot \frac{1}{2\pi\sigma_{uv} \cdot 10^3}. \quad (\text{A.6})$$

The priors used for the Bayesian fitting are reported in Table A.1.

Appendix B: Comparison of FIR sizes and flux densities derived using different methods

In Figure B.1, we compare the FIR sizes and flux densities of the rest-frame 260 μm ALMA emission, measured using four different methods: 1) fit on the image assuming a 2D Gaussian profile, 2) fit with `uvmodelfit` assuming a 2D Gaussian profile, 3) fit of the uv -visibilities assuming an exponential profile (equivalent to a Sérsic profile with $n = 1$), and 4) fit of the uv -visibilities with the ‘preferred’ model according to the BIC (point, Gaussian, exponential or Gaussian+point model, see Section 3.2). For the 2D Gaussian fit on the image plane, we show two points representing the sizes of the major and minor axis (in violet) and the mean value in magenta. For `uvmodelfit`, we show the mean value between the major and minor axis. For `cid_1057` and `cid_451`, the S/N is very low (3.6 and 5.9, respectively), therefore we do not consider their size measurements to be reliable. These two sources are highlighted with a grey band in Figure B.1.

In general, the sizes measured with different methods are in agreement within the uncertainties. We note that the sizes measured with the exponential profile are larger than the sizes measured with the Gaussian profile (factor of 1.38 on average) by construction, since the exponential profile does not decrease rapidly towards zero at larger radii and thus considers a larger amount of flux at large radii.

The flux densities are mostly insensitive to the method used. The only notable differences are for `cid_1057` and `cid_346`. `cid_1057` has a very low S/N, thus the flux measurements are not very reliable. For `cid_346`, the Gaussian fit with `uvmodelfit` measures a lower flux than the other methods. The rest-frame 260 μm emission of this galaxy is better described by a Gaussian+point source or by an exponential profile, therefore the Gaussian model cannot fit well the central flux peak and underestimates the total flux.

In Tables B.1 and B.2, we provide all the measurements obtained with the different methods. We note that when we compare our measurements to literature values in Section 5.2, we used the sizes obtained with the same method used in the literature.

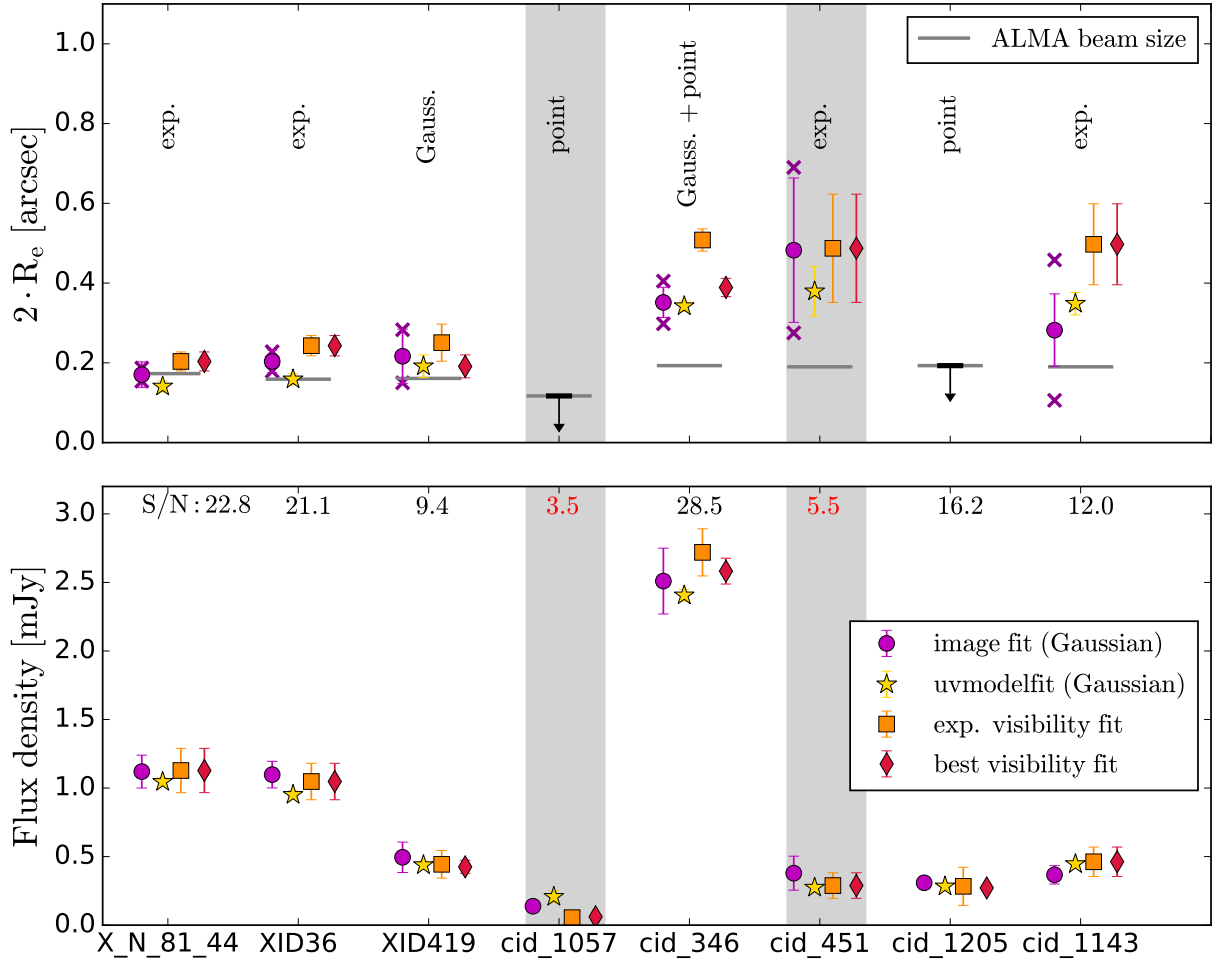


Fig. B.1. Comparison of the FIR sizes and flux densities derived using different methods: fit of a 2D Gaussian on the image plane (circles), fit of a 2D Gaussian using `uvmultifit` (stars), fit of the visibilities assuming an exponential profile (squares), and fit of the visibilities with the ‘preferred model’ according to the BIC (diamonds). The preferred model for each object is written on the top part of the figure. *Upper panel:* size measurements expressed as two times the effective radius (R_e). The grey horizontal lines represent the size of the ALMA beam for each object. For the 2D Gaussian fit on the image plane, the two magenta crosses represent the sizes of the major and minor axis. For point sources, we show the upper limit corresponding to the beam size. *Bottom panel:* integrated flux densities measured with different methods. The peak signal-to-noise (S/N) of the ALMA images is written on the top part of the panel. The results for the two objects with S/N too low to obtain reliable measurements (cid_1057 and cid_451) are highlighted with background grey shading.

Table B.1. ALMA rest-frame $260 \mu\text{m}$ (observed-frame $870 \mu\text{m}$) flux densities (F), effective radii (R_e), and ratio between major and minor axes obtained with two methods: 1) fit on the image (created with natural weighting) and 2) using `uvmodelfit`. For both methods we assume a 2D Gaussian profile. For the two point sources (cid_1057 and cid_1205), the sizes are not reported. (*) If the peak S/N < 8 in the ALMA maps, we do not consider the size measurements to be reliable.

Method:	image fit				uvmodelfit		
ID	S/N	F [mJy]	R_e [mas]	axial ratio	F [mJy]	R_e [mas]	axial ratio
X_N_81_44	22.7	1.18±0.10	98±18	1.23±0.32	1.05±0.03	70±5	1.00±0.11
XID36	21.5	1.01±0.08	99±13	1.30±0.25	0.95±0.03	79±5	1.22±0.12
XID419	9.8	0.45±0.06	112±22	1.60±0.46	0.44±0.03	96±14	2.88±0.80
cid_1057*	3.6	0.29±0.13	-	-	0.21±0.04	-	-
cid_346	29.0	2.61±0.17	186±17	1.27±0.16	2.41±0.04	171±5	1.31±0.06
cid_451*	5.9	0.35±0.08	244±66	1.91±0.76	0.27±0.02	190±36	3.15±0.83
cid_1205	16.6	0.29±0.02	-	-	0.28±0.01	-	-
cid_1143	12.1	0.56±0.07	222±36	2.49±0.60	0.45±0.02	174±18	4.60±0.70

Table B.2. ALMA rest-frame 260 μm (observed-frame 870 μm) flux densities (F) and effective radii (R_e), obtained through the fit on the visibilities using python, assuming different symmetric (i.e. axis ratio = 1) models. The model with the smallest BIC (Bayesian Information Criterion) value is the preferred model. The stars (*) mark the targets with the peak S/N < 8 in the ALMA maps, for which we do not consider the size measurements to be reliable. For point sources, we tabulate only the results of the point source model. For extended sources, we do not tabulate the result of the fit with point source model, since it gives a poor fit to the data and underestimate the fluxes. ^aFor the Gaussian+point model, we report: the total flux $F(\text{tot})=F(\text{point})+F(\text{Gaussian})$, the flux of the point source $F(\text{point})$, the half-light radius of the total profile $R_e(\text{tot})$, the half-light radius of the Gaussian component $R_e(\text{Gauss})$. ^bFor XID36 and cid_451, the difference in BIC between the exponential and Gaussian model is < 2, therefore it is not clear than one model is performing better than the other.

Model: ID	point		F [mJy]	Gaussian		F [mJy]	exponential		F(tot) [mJy]	Gauss.+point ^a			preferred model	
	F [mJy]	BIC		R_e [mas]	BIC		R_e [mas]	BIC		F(point) [mJy]	$R_e(\text{tot})$ [mas]	$R_e(\text{Gauss})$ [mas]		
X_N_81_44	-	-	1.06±0.05	75±7	80.73	1.13±0.16	102±12	74.57	1.13±0.19	0.29±0.10	84±20	111±20	77.75	exponential
XID36	-	-	0.97±0.05	86±7	51.46	1.05±0.13	122±13	50.02	0.98±0.13	0.08±0.06	90±11	96±11	55.44	exp./Gaussian ^b
XID419	-	-	0.43±0.05	96±14	42.34	0.44±0.10	125±23	45.77	0.42±0.08	0.02±0.02	97±17	101±17	47.23	Gaussian
cid_1057*	0.06±0.02	51.69	-	-	-	-	-	-	-	-	-	-	-	point
cid_346	-	-	2.41±0.08	173±7	79.40	2.72±0.17	254±14	42.91	2.58±0.14	0.35±0.05	194±11	219±11	38.77	Gauss.+point
cid_451*	-	-	0.28±0.05	194±42	45.88	0.29±0.09	244±68	45.46	0.29±0.08	0.04±0.02	212±53	236±53	47.28	exp./Gaussian ^b
cid_1205	0.27±0.02	43.71	-	-	-	-	-	-	-	-	-	-	-	point
cid_1143	-	-	0.37±0.04	140±25	54.79	0.46±0.11	249±51	47.25	0.47±0.10	0.08±0.03	221±77	257±77	53.57	exponential

Appendix C: Astrometry of the SINFONI data

In this Section, we explain the details of the registration of the astrometry of the SINFONI data-cubes. As explained in Section 4.2, the absolute position of the SINFONI cubes, as derived from the SINFONI pipeline, is not sufficiently accurate for our purposes. The small field of view of the SINFONI images (3×3 arcsec²) does not allow us to correct the astrometry using nearby stars, since usually the target is the only visible source in the field of view. Therefore, we have to derive the absolute coordinates from other images.

Reference coordinates: We use H-band and K-band images with a large field of view (3×3 arcmin²) to determine the reference coordinates of our targets that we later use to register the astrometry of the SINFONI data-cubes. We use K-band and H-band images from the VLT/VISTA and VLT/ISAAC.

To determine the coordinates from the H/K-band images, we apply the following procedure. First, we align the H/K-band images to the *Gaia* DR2 catalogue, using the Graphical Astronomy and Image Analysis Tool (GAIA) that is part of the Starlink software (Currie et al. 2014). There are at least five objects in common between the *Gaia* DR2 catalogue and each image that allow us to accurately align the images to the *Gaia* astrometry¹⁴. Then, we determine the centroid position of our target in the ‘astrometry corrected’ image by fitting a 2D Gaussian to the source.

We apply this procedure to both the H-band and K-band images. The offsets between the coordinates derived from the H-band and K-band are smaller than one pixel (< 0.07”), therefore we can assume that the H-band and K-band emission peak at the same position. We decide to use the coordinates derived from the K-band corrected images to register the astrometry of both the H-band and K-band SINFONI images.

We compare the K-band coordinates with the *Gaia* coordinates for the two objects detected in *Gaia*. For cid_346, the K-band coordinates agree very well with the *Gaia* coordinates (offset 7.3 mas). For X_N_81_44, the K-band coordinates are shifted by 0.05” to the west with respect to the coordinates from

Gaia. Given the low resolution of the K-band image for this target (FWHM PSF 1.04”), we decide to use the coordinates from *Gaia* for this source. We note that these two targets are Type 1 AGN, and are dominated by the point source emission of the AGN across the optical and near-infrared bands. Finally, we note that XID419 is only marginally detected in the K-band image (peak S/N < 6) and thus it is difficult to determine its position. Therefore for this target we rely on the coordinates derived from the *HST*/WFC3 images reported in Scholtz et al. (2020).

Registration of the SINFONI images: We use these coordinates to register the position of the peak of the emission in the SINFONI data cubes. The emission of the H/K-band filters is dominated by the continuum, but there is also some contribution from the emission lines.

For the Type 1 AGN, we check that the position of the continuum and the position derived by collapsing the total SINFONI data-cubes are in agreement, both in the H- and K-band (offset < 0.02”).

For the Type 2, the continuum is significantly detected in the SINFONI maps only in one object (XID36). For this target, we test that the position of the continuum and the position derived by collapsing the total data-cube are in agreement (offset < 0.007”), both in the H- and K-band. For the other targets, we use the SINFONI spectra to estimate the relative contribution of continuum and emission lines to the total emission in the H/K band VISTA and ISAAC filters. The continuum contribution is > 70% for all targets.

Uncertainties on the coordinate registration: The typical uncertainty on the *Gaia* coordinates is ≤ 4 mas. The precision of the alignment of the K-band images with the *Gaia* images is about half pixel (75 mas for COSMOS and 130 mas for CDF-S). The uncertainties from the 2D Gaussian fit of the VISTA or ISAAC K-band images are in the range 1-49 mas (median 4 mas). We also consider the uncertainties due to the size of the VISTA or ISAAC K-band PSF (0.78-1.04”), calculated as $\text{PSF}/(2\times\text{S/N})$ following Condon (1997), which are in the range 3-40 mas. The uncertainties on the position of the emission of the SINFONI cubes is \sim half pixel (25 mas).

To estimate the total uncertainties of the derived K-band coordinates, we added in quadrature all the above uncertainties. These uncertainties are dominated by the pixel size of the K-band images. In summary, the uncertainties on the derived SINFONI astrometry for our sample are in the range 0.03-0.14”.

¹⁴ There is an exception: cid_1205 that has only 3 sources in common between the GAIA catalogue and the H/K-band image. For this object the H/K-band position is in perfect agreement with the FIR position measured from the ALMA map, therefore we consider the H/K-band coordinates to be reliable.

Appendix D: SINFONI spectra of Type 1 AGN

Figure 3 in Section 4 shows the BLR-subtracted spectra that we used in the analysis. In this Section, we show the total SIN-

FONI emission line spectra (including the BLR component) of the three Type 1 AGN in our sample (X_N_81_44, cid_346, cid_1205).

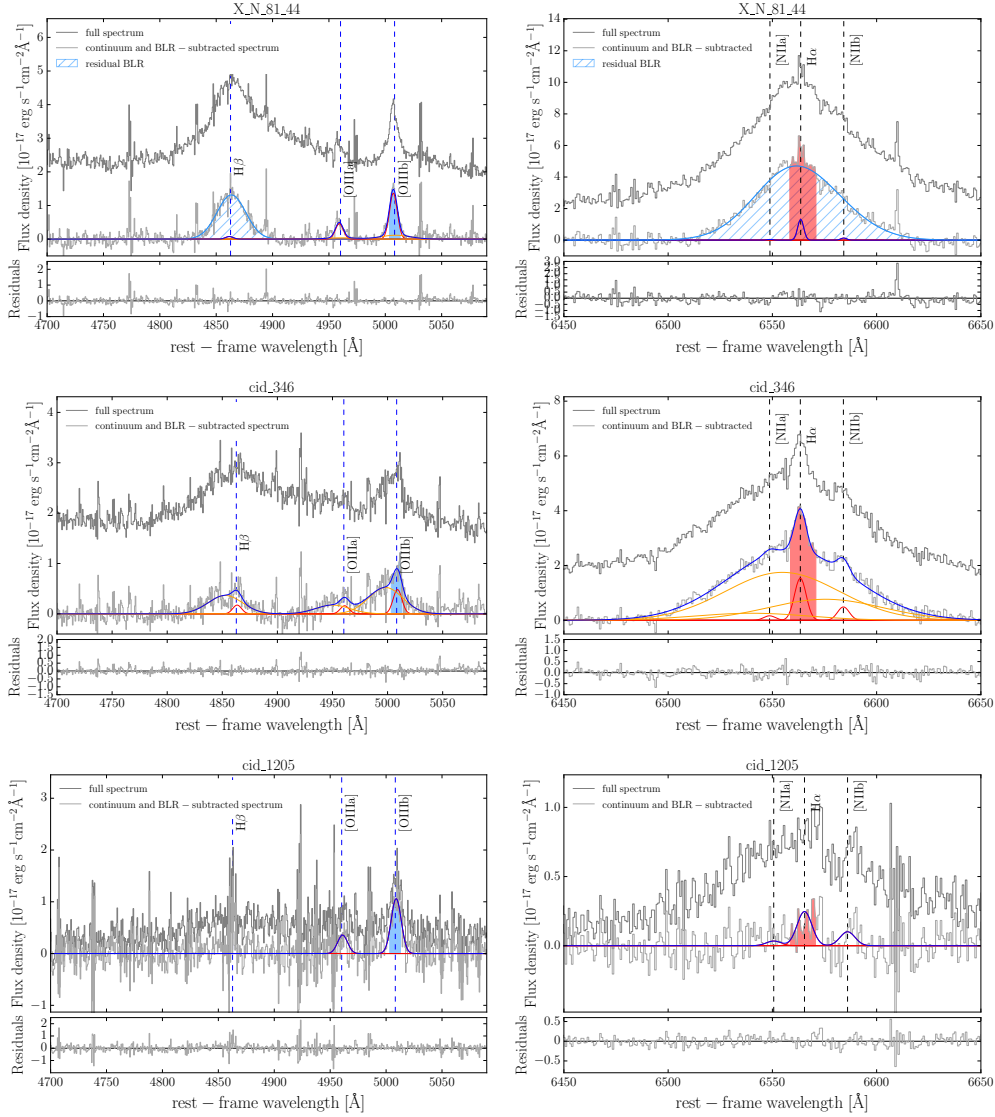


Fig. D.1. Integrated spectra of Type 1 AGN in our sample: $[\text{O III}]+\text{H}\beta$ spectra (left) and $\text{H}\alpha+[\text{N II}]$ spectra (right). The continuum- and BLR-subtracted spectra are shown in light-grey. The total spectra, before subtracting the continuum and broad line region (BLR) emission, are shown in dark grey. The blue curves show the total fit to the $\text{H}\beta$, $[\text{O III}]\lambda 4959$ and $[\text{O III}]\lambda 5007$ lines (left panel) and to the $\text{H}\alpha$, $[\text{N II}]\lambda 6548$ and $[\text{N II}]\lambda 6584$ lines (right panel). The red and orange curves show the narrow and broad components, respectively. For X_N_81_44, the broad components of the $\text{H}\beta$ and $\text{H}\alpha$ are considered as part of the BLR.

Appendix E: Spectral energy distributions (SEDs)

In Figure E.1, we show the spectral energy distributions of our targets (rest-frame wavelength range $0.1 \mu\text{m}$ – 10 cm), together with the best fit model from Circosta et al. (2018) (see description in Section 2). We use these models to predict the percentage

contribution due to dust heated by the AGN at $260 \mu\text{m}$ (rest-frame). We also show the synchrotron emission contribution at $260 \mu\text{m}$, predicted based on the available radio photometry. The different sources that can contribute to the $260 \mu\text{m}$ flux are discussed in Section 5.1.

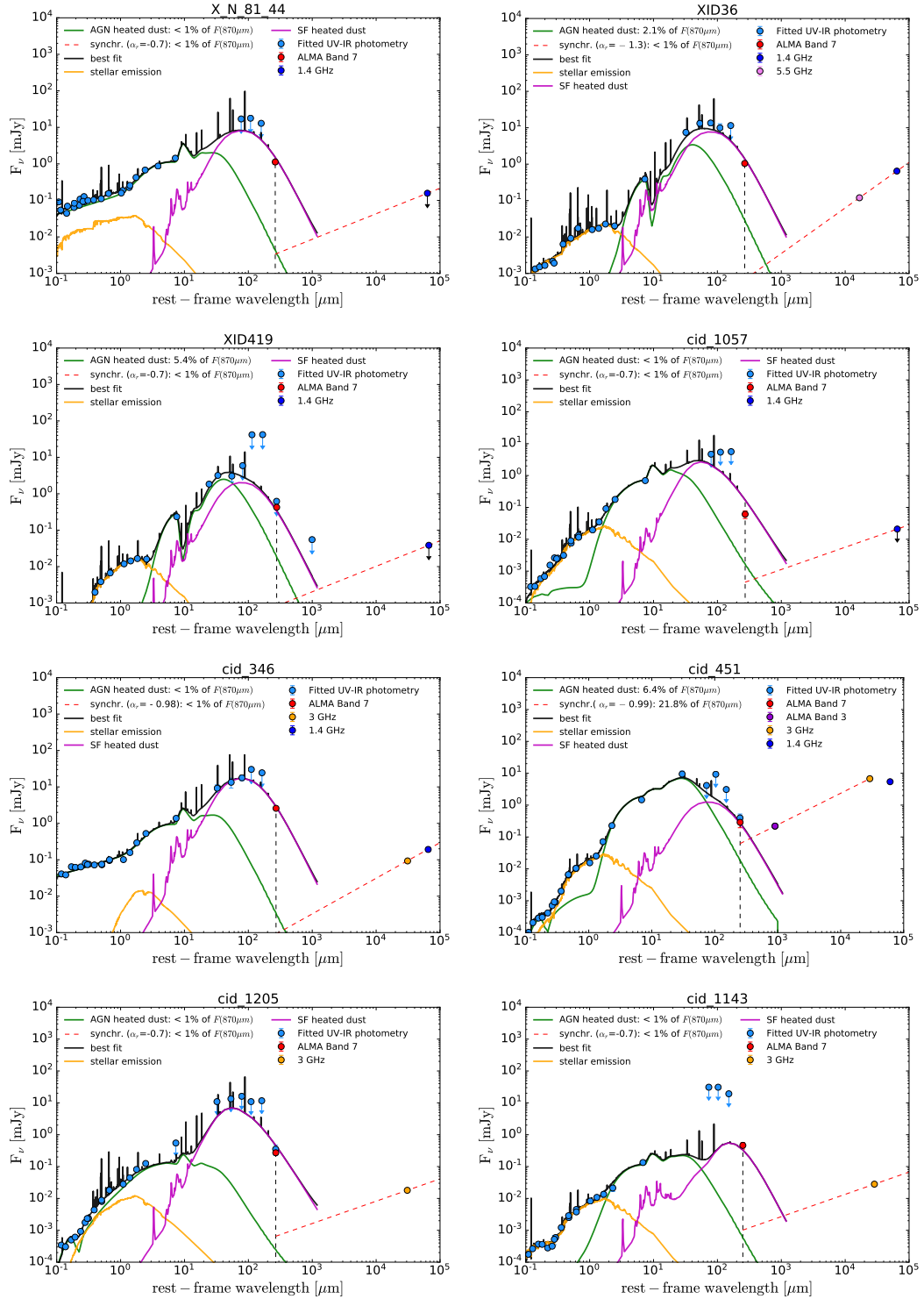


Fig. E.1. Rest-frame spectral energy distribution (SED) of our sample. The light blue data points represent the UV-IR photometry that was used for the SED fitting (Circosta et al. 2018). The red point shows our ALMA Band 7 flux measurements, which was also included in the fit. The violet point in cid_451 shows the ALMA Band 3 flux from Circosta et al. (2021). The blue, orange, and pink points show the radio fluxes at 1.4, 3, and 5 GHz, respectively. The arrows indicate 3σ upper limits. The solid curves show the results of the SED fitting with CIGALE: in black is the total best-fit model (including the contribution from the nebular emission component), in orange the dust-attenuated stellar emission, in magenta the emission from dust heated by star formation and in green the emission from dust heated by the AGN. To estimate the maximum contribution of synchrotron emission to the rest-frame $260 \mu\text{m}$ flux density we parameterized this emission as a power law with spectral index α_r (dashed red line), normalised at 3 GHz (10cm) or 1.4 GHz (21cm), depending on the available radio data. For the galaxies with radio fluxes in two bands, we derived α_r based on the two fluxes. On the plot we show the estimated contribution (in percentage) from dust heated by the AGN and from synchrotron emission to the rest-frame $260 \mu\text{m}$ ALMA Band 7 flux, estimated from the total SED template.